IL-1β+ macrophages fuel pathogenic inflammation in pancreatic cancer

(Article begins on next page)

05 February 2025

IL-1β+ macrophages fuel pathogenic inflammation in pancreatic cancer

Nicoletta Caronni # 1, Federica La Terza # 2, Francesco M Vittoria # 2 3, Giulia Barbiera # 2, Luca Mezzanzanica 2 3, Vincenzo Cuzzola 2 3, Simona Barresi 2, Marta Pellegatta 4, Paolo Canevazzi 4, Garett Dunsmore 5, Carlo Leonardi 2, Elisa Montaldo 2, Eleonora Lusito 2, Erica Dugnani 6, Antonio Citro 6, Melissa S F Ng 7, Marco Schiavo Lena 4, Denise Drago 8, Annapaola Andolfo 8, Silvia Brugiapaglia 9, Alessandro Scagliotti 9, Alessandra Mortellaro 2, Vincenzo Corbo 10, Zhaoyuan Liu 11, Anna Mondino 4, Paolo Dellabona 4, Lorenzo Piemonti 3 6, Carla Taveggia 4, Claudio Doglioni 3 4, Paola Cappello 9, Francesco Novelli 9, Matteo Iannacone 3 4, Lai Guan Ng 12, Florent Ginhoux 5 7 11 13, Stefano Crippa 3 14, Massimo Falconi 3 14, Chiara Bonini 3 4, Luigi Naldini 2 3, Marco Genua 2, Renato Ostuni 15 16

[1]San Raffaele Telethon Institute for Gene Therapy (SR-Tiget), IRCCS San Raffaele Scientific Institute, Milan, Italy. caronni.nicoletta@hsr.it.

[2]San Raffaele Telethon Institute for Gene Therapy (SR-Tiget), IRCCS San Raffaele Scientific Institute, Milan, Italy.

[3]Vita-Salute San Raffaele University, Milan, Italy.

[4]IRCCS San Raffaele Scientific Institute, Milan, Italy.

[5]INSERM U1015, Gustave Roussy Cancer Campus, Université Paris-Saclay, Villejuif, France.

[6]Diabetes Research Institute (DRI), IRCCS San Raffaele Scientific Institute, Milan, Italy.

[7]Singapore Immunology Network (SIgN), A*STAR, Singapore, Singapore.

[8]Center for Omics Sciences (COSR), IRCCS San Raffaele Scientific Institute, Milan, Italy.

[9]Department of Molecular Biotechnology and Health Sciences, University of Turin, Turin, Italy.

[10]University of Verona, Verona, Italy.

[11]Shanghai Institute of Immunology, Department of Immunology and Microbiology, Shanghai Jiao Tong University School of Medicine, Shanghai, China.

[12]Shanghai Immune Therapy Institute, Renji Hospital, Shanghai Jiao Tong University School of Medicine, Shanghai, China.

[13]Translational Immunology Institute, SingHealth/Duke-NUS Academic Medical Centre, Singapore, Singapore.

[14]Pancreas Translational and Clinical Research Center, IRCCS San Raffaele Scientific Institute, Milan, Italy.

[15]San Raffaele Telethon Institute for Gene Therapy (SR-Tiget), IRCCS San Raffaele Scientific Institute, Milan, Italy. ostuni.renato@hsr.it.

[16]Vita-Salute San Raffaele University, Milan, Italy. ostuni.renato@hsr.it.

#Contributed equally.

Abstract

Pancreatic ductal adenocarcinoma (PDAC) is a lethal disease with high resistance to therapies1. Inflammatory and immunomodulatory signals co-exist in the pancreatic tumour microenvironment, leading to dysregulated repair and cytotoxic responses. Tumour-associated macrophages (TAMs) have key roles in PDAC2, but their diversity has prevented therapeutic exploitation. Here we combined single-cell and spatial genomics with functional experiments to unravel macrophage functions in pancreatic cancer. We uncovered an inflammatory loop between tumour cells and interleukin-1β (IL-1β)-expressing TAMs, a subset of macrophages elicited by a local synergy between prostaglandin E2 (PGE2) and tumour necrosis factor (TNF). Physical proximity with IL-1β+ TAMs was associated with inflammatory reprogramming and acquisition of pathogenic properties by a subset of PDAC cells. This occurrence was an early event in pancreatic tumorigenesis and led to persistent transcriptional changes associated with disease progression and poor outcomes for patients. Blocking PGE2 or IL-1β activity elicited TAM reprogramming and antagonized tumour cell-intrinsic and -extrinsic inflammation, leading to PDAC control in vivo. Targeting the PGE2–IL-1β axis may enable preventive or therapeutic strategies for reprogramming of immune dynamics in pancreatic cancer.

Main

The diverse functions of macrophages in tissue homeostasis, immunity and cancer underlie plastic adaptations to environmental cues via the selection of genomic programmes by lineage-determining and stimulus-responsive transcription factors3,4. TAMs are relevant targets in immune oncology, as their abundance generally correlates with resistance to therapy, metastasis and poor survival. However, single-cell RNA-sequencing (scRNA-seq) studies have shown that TAMs are highly heterogenous and include subsets with diverse ontogenies, functions and therapeutic potentials2. Furthermore, macrophage activities are under local influence by cellular, physical and chemical interactions within tissue niches5.

In tumours, protective immunity triggered by sensing of cell death and danger-associated molecular patterns (DAMPs) co-exists with programmes that suppress cytotoxic responses and that stimulate tissue repair6. Exposure to these complex mixtures of signals in the tumour microenvironment (TME) underlies recurrent findings that rather than mirroring in vitro activation states, TAMs co-express genes encoding immune stimulatory, suppressive and reparative factors7,8,9. The pancreatic TME is enriched in factors that hamper the recruitment and/or activation of dendritic cells, cytotoxic natural killer (NK) cells and T lymphocytes10. By contrast, PDAC is infiltrated by resident and monocyte-derived TAMs that differentially fuel inflammation, angiogenesis and aberrant matrix deposition11,12.

Inflammatory programmes can functionally cooperate with oncogenic mutations to increase the risk of cancer development[13]. For instance, inflammatory responses to pancreatic injury trigger persistent epigenetic changes in epithelial cells that underlie non-resolving metaplasia and accelerated tumorigenesis upon subsequent Kras activation[14,15].

Here, we set out to elucidate the cellular and molecular determinants of pathogenic inflammation in pancreatic cancer.

Identification of IL-1β+ TAMs in PDAC

We performed scRNA-seq of freshly dissociated tumour samples from naive or chemotherapy-treated patients with PDAC (Supplementary Table 1). The dataset contained 59,569 single-cell transcriptomes spanning tumour, epithelial, stromal and immune compartments across patients and treatments (Extended Data Fig. 1a,b and Supplementary Table 1). Sub-clustering of mononuclear phagocytes (MNPs) uncovered subsets of TAMs whose relative abundance and gene expression programmes were largely conserved between naive and chemotherapy-treated patients (Fig. 1a and Extended Data Fig. 1c–h). SPP1+ TAMs expressed lipid metabolism (FBP1 and APOC1) and phagocytic receptor (MARCO and MERTK) genes, corresponding to previously described populations[7,8,9]; FOLR2+ TAMs expressed non-canonical myeloid marker (LYVE1 and SELENOP) genes and matched resident macrophages[11,16]; other clusters of TAMs expressed metallothionein (MT1G, MT1X and MT1E), heat-shock protein (HSP) or cell cycle (TOP2A and MKI67) genes (Fig. 1a, Extended Data Fig. 1i and Supplementary Table 1). Our analysis uncovered IL1B+ TAMs, a subset of PDAC macrophages whose transcriptome was enriched in inflammatory response (IL1B, TNF, NLRP3 and PTGS2), leukocyte recruitment (CXCL1, CXCL2 and CCL3) and angiogenesis (VEGFA, THBS1 and PDGFB) programmes but depleted of interferon response and antigen presentation Gene Ontology (GO) terms (Fig. 1b,c and Supplementary Table 1). We next computed gene signatures for TAM subsets by selecting marker genes in scRNA-seq data and filtering out non-MNP-specific transcripts. Expression of the IL1B+ TAM signature in RNA-sequencing (RNA-seq) data from The Cancer Genome Atlas (TCGA) was associated with poor patient survival, but not with overall macrophage abundance (Fig. 1d, Extended Data Fig. 1j and Supplementary Table 1). Re-analysis of bulk[17] and scRNA-seq data showed up-regulation of the IL1B+ TAM gene signature in blood monocytes from patients with PDAC, although at lower levels than in tumour-infiltrating cells (Extended Data Fig. 1k). These data uncover IL1B+ TAMs as a subset of PDAC macrophages expressing inflammatory and non-cytotoxic programmes, whose abundance correlates with poor prognosis.

IL-1β+ TAMs are conserved in mouse PDAC

We performed longitudinal scRNA-seq analyses on blood, pancreas, and tumours isolated from an orthotopic model of pancreatic cancer[18] (KrasG12D/+Trp53R172H/+ Pdx1cre/+, hereafter referred to as KPC) (Extended Data Fig. 2a–c and Supplementary Table 2). Annotation of macrophage transcriptomes revealed broad mouse–human conservation of marker genes and transcriptional programmes of Il1b+ TAMs as well as of Folr2+, Spp1+ and

Mki67+ TAMs (Extended Data Fig. 2d–f and Supplementary Table 2). These subsets were consistently identified by scRNA-seq in orthotopic or subcutaneous KrasG12D/WTPdx1cre/WT (hereafter KC) models, or in autochthonous tumours from KPC mice (Extended Data Fig. 2g and Supplementary Table 2). Having observed an early and persistent accumulation of Il1b+ TAMs in mouse PDAC (Fig. 1e), we set out to characterize the phenotype of these cells. In keeping with scRNA-seq analyses, IL-1β was expressed by a subset of TAMs in PDAC but not by pancreatic macrophages from control mice (Fig. 1f). Mouse IL-1β+ TAMs expressed CD64, CD11c, major histocompatibility complex class II (MHCII) and the costimulatory molecules CD80 and CD86, together with markers of immune dysfunction in cancer such as CD206, arginase 1 (ARG1) and the immune checkpoint inhibitor PD-L1 (Fig. 1g and Extended Data Fig. 2h). Thus, IL-1β+ TAMs are a conserved macrophage population that co-expresses inflammatory and immune inhibitory markers.

A monocytic origin of IL-1β+ TAMs

Data from scRNA-seq of mouse monocytes and macrophages from blood, pancreas and tumours were integrated and subjected to optimal transport analysis to infer ancestor–descendant relationships[19]. We found that IL-1β+ TAMs had a higher probability of being derived from monocytes than bona fide resident Clps+ or Folr2+ macrophages (Extended Data Fig. 3a–j). CellRank analyses[20] also uncovered a trajectory linking tumour-infiltrating monocytes and IL-1β+ TAMs, with key marker genes of IL-1β+ TAMs (Il1b, Ptgs2 and Cxcl2) driving the predicted transition (Fig. 2a,b, Extended Data Fig. 3k and Supplementary Table 3). Monocytes entering the tumour readily up-regulated these transcripts and progressively acquired IL-1β+ TAM identity in mouse and human PDAC (Fig. 2c and Extended Data Fig. 3l). Accordingly, protein levels of IL-1β were low in circulating monocytes from control and tumour-bearing mice but increased substantially upon recruitment to tumours (Fig. 2d). We next performed lineage tracing with Ms4a3cre-RosaTdT mice, in which granulocyte-monocyte precursors (GMP) and their progeny are irreversibly marked by tdTomato[21]. The vast majority of IL-1β+ TAMs were tdTomato+ (Fig. 2e), indicating that these cells originate from circulating monocytes that infiltrate the tumour and become exposed to local factors in the TME.

PGE2 and TNF elicit IL-1β+ TAMs

We observed an enrichment of IL-1 and TNF response GO terms among driver genes of the monocyte-to-IL-1β+ TAM transition (Extended Data Fig. 4a and Supplementary Table 3). The transcriptome of IL-1β+ TAMs was enriched in genes induced by IL-1β or TNF in mouse macrophages[22], and both molecules were detectable in human PDAC (Extended Data Fig. 4b,c and Supplementary Table 4). However, treatment of mouse bone marrow-derived macrophages (BMDMs) with IL-1β or TNF did not elicit IL-1β synthesis, highlighting a requirement for additional factors (Extended Data Fig. 4d). The eicosanoid PGE2, a known regulator of the immune TME[23], can stimulate IL-1β production while suppressing interferon responses in macrophages[24,25,26]. We detected high levels of PGE2 in biopsies of human

and mouse PDAC or in culture supernatant of tumour cells, and PGE2-induced genes[25] were over-represented in IL-1β+ TAMs (Fig. 2f, Extended Data Fig. 4e,f and Supplementary Table 4). We thus tested whether PGE2 contributed to elicit the IL-1β+ TAM state. PGE2 alone had limited effects, but its co-administration with TNF—and not with IL-1β—triggered potent IL-1β synthesis in BMDMs and monocytes (Fig. 2g and Extended Data Fig. 4g,h). RNA-seq analyses in BMDMs identified dozens of transcripts synergistically induced by PGE2 plus TNF, which were over-represented in IL-1β+ TAMs and among the driver genes of monocyte-to-IL-1β+ TAM transition; these genes encoded for factors that elicit tumour-promoting inflammation (Il1b and Il6) while suppressing cytotoxic immunity (Il10), or that stimulate prostaglandin synthesis (Ptges and Ptgs2), myeloid cell recruitment (Cxcl1, Cxcl2 and Cxcl3) and tissue repair (Areg, Arg2, Wnt11 and Il33) (Fig. 2h–j and Supplementary Table 4). Multiplexed analyses of proteins in the supernatant confirmed elevated synthesis of IL-6 and IL-10 by co-stimulated macrophages, and revealed PGE2-driven suppression of CCL5, CXCL10, CXCL11 and CXCL16—chemokines with key roles in recruitment of cytotoxic T and NK cells (Fig. 2k). These data identify PGE2 and TNF as TME factors that are able to cooperatively elicit the IL-1β+ TAM state in PDAC.

IL-1β+ TAMs accumulate in hypoxic areas

Immunofluorescence analyses of orthotopic PDAC highlighted a preferential distribution of IL-1β+ TAMs in fibroblast-rich stromal regions surrounding the tumour core; differential distribution of TAM subsets was detectable at early time points in mouse tumours as well as in human PDAC (Extended Data Fig. 5a–c). We next performed paired single-cell and spatial transcriptome analyses of mouse PDAC. Transcript-based deconvolution of cell subsets was concordant with protein expression (Extended Data Fig. 5d–g and Supplementary Table 5). Spatial principal components (sPC) analyses discriminated spots enriched in IL-1β+, FOLR2+ or SPP1+ TAMs (Extended Data Fig. 5h–k). Projection of signatures of genes synergized by PGE2 plus TNF showed broad overlap with spots enriched in IL-1β+ TAMs (Extended Data Fig. 5l). IL-1β+ TAM regions were enriched in GO terms associated with inflammation, hypoxia, angiogenesis and wound healing (Extended Data Fig. 5m,n and Supplementary Table 5), as validated by immunofluorescence analyses showing the proximity of IL-1β+ TAMs to CD31+VEGFR2+ endothelial cells and hypoxic areas (Extended Data Fig. 5o–p). We conclude that IL-1β+ TAMs undergo local specification in inflamed, angiogenic and hypoxic regions of PDAC associated with high PGE2 and TNF synergistic activity.

PDAC-derived PGE2 promotes tumour growth

To assess the role of PGE2 in PDAC, we treated immune-competent mice with celecoxib, a selective inhibitor of the prostaglandin biosynthetic enzyme cyclo-oxygenase-2 (COX2), concomitant with tumour challenge. This treatment lowered PGE2 levels in tumours and was associated with reduced accumulation of IL-1β+ TAMs and monocytes, increased infiltration of cytotoxic GZMB+CD8+ T cells and delayed tumour growth (Extended Data Fig. 6a–d). Because cancer cells produce high levels of PGE2 (Extended Data Fig. 4e), we generated COX2-knockout (KO) PDAC lines that were unable to produce PGE2 but did not show defects

in viability or proliferation in vitro (Extended Data Fig. 6e–h and Supplementary Table 6). COX2-KO PDAC cells or spheroids engrafted in immune-competent mice but their growth was controlled in a CD8+ T cell- and NK cell-dependent manner, in keeping with an observed increase of lymphocyte activation in tumour-draining lymph nodes (Fig. 3a,b and Extended Data Fig. 6i,j). Although neutrophil frequencies were reduced, immune cell composition was largely comparable between control and COX2-KO tumours at early disease stages (Extended Data Fig. 6k). We next performed scRNA-seq to assess the effect of PGE2 on the pancreatic TME and found marked gene expression changes in selected cell populations, such as macrophages, activated T cells and fibroblasts (Extended Data Fig. 6l,n and Supplementary Table 6). More specifically, IL-1β+ TAMs isolated from COX2-KO tumours showed reduced expression of key identity genes and inflammatory response markers and acquired interferon response signatures (Fig. 3c and Extended Data Fig. 6o). COX2-KO tumours were, however, controlled in mice lacking a key subunit of the IFNα and IFNβ receptor (Ifnar1−/− mice) (Extended Data Fig. 6p). These data identify a key role of tumour-derived PGE2 in driving the IL-1β+ TAM state in vivo and show that targeting COX2 leads to TME reprogramming and disease control in an interferon-independent manner.

Pathogenic IL-1β signalling in PDAC cells

Antibody-mediated targeting of IL-1β in vivo led to delayed PDAC growth, concomitant with reduced IL-1β expression by monocytes and TAMs and increased activation of cytotoxic T cells in draining lymph nodes (Fig. 3d–f and Extended Data Fig. 7a–c). Re-analysis of patient scRNA-seq data highlighted tumour monocytes and IL1B+ TAMs as the major sources of IL-1β in human PDAC (Extended Data Fig. 7d and Supplementary Table 1). To determine the cellular targets of IL-1β in the TME, we performed tumour challenge experiments in haemato-chimeric mice in which bone marrow cells from Il1r1−/− donors, which lack a key signalling subunit of the IL-1 receptor, or from wild-type control were transplanted into irradiated wild-type or Il1r1−/− recipients, respectively. No defect in tumour growth was observed in the two groups (Extended Data Fig. 7e), indicating that the cancer-promoting effects of IL-1β are not driven by signalling in haematopoietic or stromal cells. Instead, IL1R1-KO KPC cells showed a markedly reduced capacity to form tumours in immune-competent mice, concomitant with reduced infiltration of IL-1β+ monocytes and increased activation of CD8+ T cells (Fig. 3g, Extended Data Fig. 7f–i and Supplementary Table 7). Re-expression of IL1R1 in gene-targeted PDAC cells rescued tumour growth in vivo (Fig. 3h and Extended Data Fig. 7j). Finally, stimulation with IL-1β promoted organoid generation by control PDAC cells, and not by IL1R1-KO PDAC cells, and explants of IL1R1-KO tumours showed defective organoid-forming efficiency (Fig. 3i and Extended Data Fig. 7k). These data highlight a requirement for tumour cell-intrinsic IL-1β signalling for PDAC growth.

Inflamed PDAC and TAMs engage in a loop

RNA-seq analyses of KPC cells treated with IL-1β revealed marked up-regulation of genes encoding myeloid growth factors (Csf1 and Csf2), chemokines (Ccl2), cytokines (Tnf) and enzymes with immune regulatory functions (Ptgs2 and Nos2) (Extended Data Fig. 8a and

Supplementary Table 8). These results were confirmed by quantification of proteins in the supernatant, with CCL2 and CSF-1 being robustly induced by IL-1β in tumour cells (Extended Data Fig. 8a). To assess the functional relevance of these molecules, we performed tumour challenge experiments in Ccr2−/− mice, which lack the CCL2 receptor, and in wild-type mice treated with a neutralizing antibody against CSF-1. Both experiments led to impaired disease growth, highlighting a key role of monocyte-derived macrophages in PDAC (Extended Data Fig. 8b). We next focused on IL-1β-induced factors that drive macrophage conditioning. Among the most enriched GO terms in the transcriptome of cytokine-treated tumour cells were those associated with inflammation and prostaglandin secretion, in line with the finding that stimulation of KPC cells with IL-1β led to increased production of PGE2 and TNF (Extended Data Fig. 8a,c and Supplementary Table 8). We next performed supernatant transfer experiments whereby tumour-conditioned medium (TCM) from KPC cells treated with IL-1β in the absence or presence of COX2 inhibitor (COX2i) were incubated with a blocking antibody against TNF and subsequently transferred onto BMDMs. Whereas TCM from untreated KPC cells did not trigger Il1b in macrophages, this gene was induced in response to TCM of IL-1β-stimulated tumour cells (Extended Data Fig. 8d). Inhibition of COX2 in KPC cells treated with IL-1β led to lower induction of Il1b in BMDMs exposed to the corresponding TCM, with this occurrence being even more evident upon neutralization of TNF (Extended Data Fig. 8d). These data highlight a self-sustaining loop between PDAC cells and macrophages, whereby IL-1β signalling in tumour cells triggers the release of factors that recruit monocytes to tumours and elicit the IL-1β+ TAM state.

Early inflammatory reprogramming of PDAC

We integrated RNA-seq data from cytokine-treated PDAC cells and organoids to define a tumour-intrinsic IL-1β response signature (T1RS) (Extended Data Fig. 9a,b and Supplementary Table 9). This gene module was enriched in mouse15 and human27 PDAC transcriptomes, and it correlated with abundance of IL-1β+ TAMs and poor survival in TCGA (Fig. 4a, Extended Data Fig. 9c and Supplementary Table 9). Longitudinal scRNA-seq analyses of orthotopic PDAC revealed up-regulation of T1RS in tumour cells at early time points, anticipating exponential disease growth and acquisition of proliferation, epithelial-to-mesenchymal transition (EMT) and extracellular matrix remodelling programmes (Extended Data Fig. 9d,e). To assess inflammatory reprogramming of tumour cells in vivo, we analysed gene expression data from mouse models of pancreatic tumorigenesis28. These studies revealed the highest T1RS expression in cells from mice with benign pancreatic intraepithelial neoplasia (PanIN), with levels of the signature remaining high in established PDAC and distal metastasis (Fig. 4b). Spatial transcriptome data from donor and patient samples29 confirmed robust expression of the T1RS genes in human PanIN and PDAC lesions (Extended Data Fig. 9f). Inflammatory responses to tissue damage functionally cooperate with oncogenes to enhance pancreatic tumorigenesis via long-term reprogramming of epithelial cells14,15. We detected a subset of macrophages from patients with hereditary or idiopathic chronic pancreatitis30 displaying a gene expression programme analogous to that of IL-1β+ TAMs (Extended Data Fig. 9g,h). Analysis of RNA-seq data of normal or Kras-mutated cells from mice with caerulein-driven pancreatitis revealed marked T1RS expression as a consequence of oncogene

activation, with levels of the module further increased upon injury (Fig. 4b). Analogous findings were obtained in cells from mice treated with the alarmin IL-33, which mediates tissue damage responses in the pancreas15 (Extended Data Fig. 9i). Furthermore, T1RS expression remained elevated in pancreatic spheroids generated from caerulein-treated mice months after resolution of the injury14 (Extended Data Fig. 9i). Thus, inflammatory reprogramming is an early event in pancreatic tumorigenesis leading to persistent transcriptional changes associated with disease progression and poor patient outcome.

IL-1β+ TAMs colocalize with T1RS+ PDAC

We next explored whether local interactions with IL-1β+ TAMs underlie transcriptional heterogeneity and inflammatory reprogramming of tumour cells. Analysis of scRNA-seq data from patients with PDAC uncovered a subset of cancer cells expressing high levels of the T1RS (Fig. 5a, Extended Data Fig. 10a and Supplementary Table 10). Pseudotime analyses31 identified T1RS+ PDAC cells as endpoints of a transcriptional trajectory driven by increasing expression of the T1RS itself and of known IL-1β target genes, such as NFKBIA, IL1RN and CXCL1 (Fig. 5a–c and Supplementary Table 10). The predicted development of T1RS+ PDAC cells was also associated with increased expression of tumour markers (CEACAM6, CEACAM7 and KRT19) and enrichment of GO terms associated to pancreatic tumorigenesis such as KRAS signalling, hypoxia, EMT, p53 pathway and TGFβ signalling, among others (Fig. 5c,d and Supplementary Table 10). These data highlight an intrinsic correlation between inflammatory reprogramming and acquisition of pathogenic programmes by tumour cells. We next set out to identify local interactions between macrophages and tumour cells using single-cell spatial gene expression in human PDAC. These analyses identified IL-1β+ TAMs, as well as subsets of macrophages, immune, epithelial and stromal cells. We also detected putative T1RS+ PDAC cells characterized by expression of KRT19 and CXCL1 and weak positivity for IL1B (Fig. 5e, Extended Data Fig. 10b and Supplementary Table 10). Overall, there was a clear spatial co-expression of CXCL1 with KRT19 and genes marking macrophages (CD68), as well as IL-1β (IL1B, IL1A and THBS1) and PGE2 (PTGS2 and PTGER1) programmes; correlation values were higher for marker genes of IL-1β+ TAMs than for other macrophage subsets (Extended Data Fig. 10c and Supplementary Table 10). Indeed, T1RS+ PDAC cells and IL-1β+ TAMs were significantly and selectively enriched in each other's spatial neighbourhoods (Fig. 5f,g and Extended Data Fig. 10d,e). Ligand–receptor interaction analysis32 between tumour cells and IL-1β+ TAMs identified the IL-1–IL1R1 axis as the top-ranking driver of T1RS+ PDAC cell gene expression (Fig. 5h and Extended Data Fig. 10f–h). These data highlight a spatially confined crosstalk between IL-1β+ TAMs and T1RS+ PDAC cells sustained by the PGE2–IL-1β axis.

Discussion

Tissue-resident macrophages contribute to PDAC development and progression[11,12]. Here we report a pathogenic role of IL-1β+ TAMs—a subset of monocyte-derived macrophages endowed with inflammatory, but not cytotoxic, programmes—in pancreatic cancer. IL-1β+ TAMs engage in a spatially confined interaction with a subset of PDAC cells expressing an IL-1β response signature (T1RS) associated with poor patient survival. Our data indicate that tumour-infiltrating monocytes differentiate into IL-1β+ TAMs upon exposure to PGE2 and TNF and drive inflammatory reprogramming of neighbouring PDAC cells, promoting synthesis of PGE2, TNF and other factors that further reinforce the IL-1β+ TAM state. Local elicitation of a positive feedback loop between IL-1β+ TAMs and T1RS+ PDAC cells maintains a functional TME niche despite the labile biological activities of inflammatory mediators[33,34]. In this context, that T1RS+ PDAC cells express genes of the IL-1β+ TAM programme—CXCL1 and, at low levels, IL1B itself—highlights spatially coordinated gene expression programmes across cell types in the TME, in line with a recent report[9]. Our data establish the PGE2–IL-1β axis as a driver of the spatial and transcriptional heterogeneity of immune and tumour cells in PDAC.

The biological effects of PGE2—suppression of cytotoxic immunity and enhancement of tumour-promoting inflammation[35]—reflect divergent control of gene modules in macrophages. PGE2 limits interferon responses by targeting MEF2A and promoting IL-10 release[25], while boosting expression of inflammatory factors with roles in tissue repair, such as IL-1β. The molecular mechanisms underlying PGE2-mediated synergisms remain to be elucidated. We found that IL-1β+ TAMs accumulate in hypoxic areas of the tumour where inflammation, tissue repair and immune suppression co-exist[36]. In this context, PGE2 was found to stabilize HIF-1α[37], a transcription factor that drives IL-1β synthesis in macrophages[38]. Future studies should examine whether and how hypoxia or other factors, such as physical tension or local interaction with stromal cells such as fibroblasts[39], contribute to the establishment or maintenance of IL-1β+ TAM niches.

Inflammatory signalling in epithelial cells sustains tissue repair but can enhance tumorigenesis upon oncogene activation[14,15]. Reciprocally, driver mutations that accumulate in healthy tissues may never give rise to tumours in the absence of sustained injury[13]. Macrophages from patients with pancreatitis acquire a gene expression programme analogous to that of IL-1β+ TAMs, possibly sustained by PGE2 released from damaged cells[40]. Furthermore, Kras mutations are sufficient to trigger PGE2 synthesis[23] and T1RS expression in epithelial cells, at levels that are increased upon tissue injury. Elicitation of a self-feeding loop via the PGE2–IL-1β axis would thus integrate and stabilize the consequences of tissue injury and activated oncogenes.

The pathogenic effects of inflammation in mutated cells underlie the resurgence of stem cell programmes, lineage infidelity or increased cell fitness[13]. We observed that inflammatory reprogramming of PDAC was required for disease growth and organoid formation, and it was

associated with the acquisition of pathologic programmes such as EMT, in keeping with recent reports in kidney cancer[41,42]. We posit that activation of the PGE2–IL-1β axis represents a physiological response to injury whose co-optation by cancer promotes disease progression.

The work described in this Article and other studies[43,44,45,46,47,48] establish the PGE2–IL-1β axis as a driver of tumour-promoting inflammation. Although macrophages are a key source of IL-1β in pancreatic cancer, subsets of tumour cells[43]—namely, T1RS+ PDAC cells—or other populations in the niche may also contribute to cytokine synthesis, highlighting broad targeting of the pathway as a strategy to overcome compensatory effects. Given the self-amplifying nature of the loop, inhibition of the PGE2–IL-1β axis should have maximal therapeutic efficacy during early stages or in preventive settings, while boosting immunotherapy in advanced disease[46,47,48].

Targeting IL-1β might yield variable therapeutic outcomes according to the cell type- and tissue-specific activities of this cytokine[46]. Indeed, IL-1β supports cytotoxic T cell activation in tumour-draining lymph nodes[49] and the CANTOS trial in patients treated with the IL-1β blocking antibody canakinumab showed a reduced incidence of lung, but not colorectal, cancer[50]. Having resolved the molecular, spatial and functional regulation of IL-1β+ TAMs, our study should inform the design and interpretation of clinical trials targeting IL-1β and/or COX2 as preventive or combination immunotherapies.

Methods

Patient samples

Human samples from resected primary PDAC as well as peripheral blood samples were obtained from the Pancreatic Surgery Unit at the Pancreas Translational and Clinical Center of San Raffaele Hospital (Milan, Italy). The study was compliant with the Declaration of Helsinki and the General Data Protection Regulation and was approved by San Raffaele Hospital ethic committee (protocols: NEU-IPMN and LiMeT). Tissue specimens were confirmed to be tumour or adjacent normal tissue based on pathologist assessment. Informed consent was obtained by all participants, which received no compensation. Age and sex, as well as anonymized clinical information of participants are reported in Supplementary Table 1.

Mouse PDAC

KC (DT6606) and KPC (K8484) cell lines were previously established[18,51,52] from tumours arising in genetically engineered mouse models (GEMMs) carrying the G12D oncogenic mutation in the Kras gene (KrasLSL-G12D/+;Pdx1cre/WT for KC) and the missense point R720H mutation in the Tpr53 gene (KrasLSL-G12D/+;Tpr53LSL-R270H/+;Pdx1cre/WT for KPC). Panc02 cell line is derived from a methylcholanthrene-induced PDAC[53]. KC, KPC and Panc02

cell lines were kindly provided by L. Piemonti and not authenticated. All cell lines were cultured under standard conditions and periodically tested for mycoplasma.

CRISPR–Cas9-mediated gene targeting

Single guide RNAs (sgRNAs) were designed using CHOPCHOP54 and synthetized by in vitro transcription using GeneArt Precision gRNA Synthesis Kit (Invitrogen), following manufacturer's instructions. Ribonucleoprotein complexes (Cas9–sgRNA) were generated by incubating 12 µg of sgRNA with 5 µg of Cas9 for 15 min at room temperature. KPC, KC or Panc02 cells ($2.5 × 10^4$) were resuspended in SF solution of SF Cell Line 4D Nucleofector X Kit S, mixed with ribonucleoprotein complexes and electroporated using EP-100 program of the 4D Nucleofector System (Lonza). Three days after nucleofection, single clones were sorted by fluorescence-activated cell sorting (FACS) in 96-well plates. Single-cell clones were screened to evaluate non-homologous end joining (NHEJ) efficiency on the targeted site with T7 endonuclease assay. In brief, genomic DNA was extracted using QuickExtract DNA Extraction Solution and targeted regions were amplified by PCR. PCR products were purified with Ampure XP beads and quantified by Nanodrop 8000. Purified PCR products were mixed 1:1 with corresponding products from wild-type cells. Annealed PCR products (400 ng) were digested with T7 Endonuclease for 30 min at 37 °C and subjected to capillary electrophoresis using D1000 TapeStation kit (Agilent 4200 TapeStation). NHEJ efficiency was defined by calculating the percentage of PCR product cleavage. Gene-edited clones were validated by Sanger sequencing using PCR products encompassing the target sequence. Polyclonal knockout pools were generated mixing an equal amount of at least five validated clones. The absence of the targeted protein was further validated by western blot analyses. A complete list of sgRNAs and primer pairs used for the NHEJ assay is reported in the Supplementary Tables 6 and 7.

In vivo animal studies

All experiments and procedures were performed according to protocols approved by the Institutional Animal Care and Use Committee (IACUC) at San Raffaele Scientific Institute animal facilities and authorized by the Italian Ministry of Health in accordance with the Italian Laws (D.L.vo 116/92), which enforce the EU 86/609 Directive (approval numbers 449/2018-PR, 962/2020-PR and 908/2021-PR). C57BL/6 N mice were purchased from Charles River Italy; IFNAR-KO and CCR2-KO mice were obtained from Matteo Iannacone (IRCCS San Raffaele Scientific Institute, Milan, Italy); IL1R1-KO mice were provided by C. Garlanda. All mice were maintained under pathogen-free conditions at the animal facility of San Raffaele Scientific Institute with a 12 h:12 h dark:light cycle and standardized temperature (22 ± 2 °C) and humidity (55 ± 5%). Ms4a3cre-RosaTdT mice were maintained under pathogen-free conditions at Institute Gustave Roussy. Pancreatic tissue samples from GEMMs of PDAC (KrasLSL-G12D/+;Tpr53LSL-R270H/+;Pdx1cre/WT) were provided by F. Novelli. No statistical method was used to predetermine sample size. Sample sizes were estimated based on preliminary experiments. Mice were allocated randomly to the experimental groups. Blinding was used to measure tumour growth curves, both when using digital calliper and ultrasound analyses.

Orthotopic tumours

To establish orthotopic models, 6- to 9-week-old female (KPC injection) and male (KC injection) mice were anaesthetized with isoflurane and subjected to surgical procedure. After left abdominal incision, pancreatic tails were exposed and injected with 5×10^5 tumour cells resuspended in cold PBS mixed at 1:4 dilution with Matrigel (Corning) in a final volume of 50 µl. Mice were monitored with ultrasound imaging to measure tumour progression. Experiments were terminated when tumours reached a size of 1,000 mm3, as per the IACUC limit.

Heterotopic tumours

To establish heterotopic tumours, a total of 2×10^6 cancer cells were resuspended in 200uL of endotoxin-free PBS and injected subcutaneously in the right flank of mice. Female mice were used for KPC injection and male mice were used for KC and PANC02 injection. Tumour growth was monitored using a digital caliper. Tumour volume was estimated assuming ellipsoidal shape as $(a \times b)2 \times \pi/6$, where a is the major diameter and b is the minor diameter. Experiments were terminated when tumours reached a size of 1,000 mm3, as per IACUC limit.

In vivo treatments

The COX2 inhibitor celecoxib was prepared at a concentration of 2 mg ml−1 in a solution of 10% DMSO, 50% poly(ethylene glycol) (Average Mn 400 (PEG400) (Sigma)), and 40% Cell Culture Grade Water (Corning) and 200 µl (400 µg per mouse) were administered daily through oral gavage55. For IL-1β neutralization, mice were intraperitoneally injected with 50 µg per mouse of IL-1β monoclonal antibody (Clone B122, InVivoMAb, BioXCell) or isotype control (Polyclonal Armenian Hamster IgG, InVivoMAb, BioXCell) on the day of tumour inoculation and at 1 day post inoculation (dpi). Starting from day 4 dpi, mice were injected three times a week for the entire duration of the experiment. CD8+ T cells depletion was achieved by injecting mice intraperitoneally with 300 µg per mouse of anti-mouse CD8α (Clone 2.43, BioXCell) or isotype control (Clone LTF-2, BioXCell) 2 days before tumour injection. Starting from day 4 dpi, mice were treated twice a week with 200 µg per mouse of antibody or isotype control for the entire duration of the experiment. Depletion of CD8+ T cells was confirmed by FACS analysis on blood and tumour samples. NK cells depletion was achieved by injecting the mice with a combination of 200 µg per mouse of anti-mouse NK1.1 (clone PK136, BioXCell) and 50 µl per mouse of anti-ASIALO GM-1 (clone Poly21460, BioLegend) or isotype control (clone C1.18.4, BioXCell) 1 day before and 1 day after tumour inoculation. Starting from day 4 dpi, mice were injected twice a week for the entire duration of the experiment. Depletion of NK cells was confirmed by FACS analysis on blood and tumour samples. For CSF-1 neutralization, mice were intraperitoneally injected with 1 mg/mouse of mouse CSF-1 monoclonal antibody (Clone 5A1, BioXCell) or isotype control (clone HRPN, BioXCell) 3 days before tumour inoculation. Starting from day 1 dpi, mice were injected with 500 µg per mouse

every 5 days. Depletion of monocytes was assessed by FACS analysis on blood and tumour samples.

Bone marrow chimeras

Recipient mice were lethally irradiated with two doses of radiations for a total of 935 cGy. The following day, irradiated mice were transplanted with 5 × 106 total bone marrow cells by intravenous injections. Bone marrow chimerism was checked by measuring the percentage of CD45.1/CD45.2 cells in blood samples by flow cytometry 4- and 10-weeks post transplantation. Bone marrow chimeras were inoculated with KPC cells 12-weeks post transplantation.

Tissue processing

Human and mouse peripheral blood samples were incubated with red blood cell (RBC) lysis buffer (Biolegend) for 10 min on ice and washed with PBS. Cells were centrifuged for 5 min at 450g and resuspended in the appropriate buffer for downstream application. Freshly resected human PDAC samples were minced in small pieces and digested with the Tumor Dissociation Kit, Human (Miltenyi Biotec). Similarly, mouse healthy pancreas and tumours were manually minced in small pieces and dissociated with the Tumor Dissociation Kit, Mouse (Miltenyi Biotec) following the manufacturer's instructions. The obtained single cells suspensions were filtered on 70-μm cell strainers, incubated with RBC lysis buffer for 10 min on ice and resuspended in the appropriate buffer for cell counting and downstream application. In selected experiments, mouse tumour-draining lymph nodes were smashed, filtered through a 70-μm cell strainer, and resuspended in the appropriate buffer for downstream application. For the collection of plasma samples, an aliquot of 300 μl of blood collected into EDTA tubes was centrifuged for 5 min at 10,000g. Plasma was transferred into a clean tube and re-centrifuged 5 min at 10,000g. Plasma samples were frozen and stored at −80 °C until use. Supernatants of human PDAC and normal adjacent tissues were generated by culturing weighted tissues (1 to 30 mg) in 1 ml of complete media in a 48-well plate. After 48 h, supernatants were collected, centrifuged for 5 min at 450g to remove cellular debris and stored at −80 °C until use. For mass spectrometry experiments, tissue samples were chopped, weighted and immediately snap frozen at −80 °C.

Culture of mouse monocytes and macrophages

Bone marrow cells were collected by crushing the hips, femurs, and tibias of female mice in 50 ml of sterile PBS, filtered through a 70-μm cell strainer, and centrifuged for 5 min at 450g. Red blood cells were lysed using 0.2% NaCl solution, followed by 1.6% NaCl solution. Bone marrow cells were filtered through a 70-μm cell strainers and centrifuged for 5 min at 450g. For BMDM differentiation, cells were counted and seeded in IMDM supplemented with 20% FBS, 20% L929-conditioned media containing M-CSF, antibiotics (penicillin G 100 U ml−1 and streptomycin sulfate 100 U ml−1), 2 mM l-glutamine and 5 μM 2-mercaptoethanol. Four days

after culture, fresh medium was added to the cells. At day 7 after plating, cells were stimulated as described below. Monocytes were isolated from total bone marrow cells using the mouse Monocyte Isolation Kit (BM, Miltenyi Biotec), following manufacturer's instructions. At the end of the isolation procedure, cells were >90–95% CD11b+Ly6G−Ly6C+ as assessed by flow cytometry. Monocytes were counted and seeded in U-bottom 96-well plates at a density of 1 × 10⁵ cells per well in RPMI supplemented with 10% FBS, antibiotics (penicillin G 100 U ml−1 and streptomycin sulfate 100 U ml−1) and 2 mM l-glutamine. One hour after plating, monocytes were stimulated as described below.

Ex vivo stimulation of mouse cells

Cells were stimulated with TNF (10 ng ml−1), PGE2 (1 µM) and/or IL-1β (10 ng ml−1). For stimulation with TCM, KPC cells were stimulated or not for 24 h with either IL-1β (10 ng ml−1), COX2 inhibitor SC-236 (Cayman Chemical) (10 µM), or both. At the end of the stimulation, TCM was collected, centrifuged for 5 min at 450g to remove cellular debris, filtered through 0.22-µm strainer and stored at −80 °C. Before BMDM stimulation, thawed TCM was incubated at 37 °C for 30 min with anti-TNF (25 µg ml−1; Clone XT3.11, InVivoMAb, BioXCell) or isotype control rat IgG1 anti-horseradish peroxidase (25 µg ml−1; Clone HRPN, InVivoMAb, BioXCell). To rule out any carryover effect of COX2 inhibitor, fresh SC-236 (10 µM) was added to the TCM before stimulating BMDMs.

Generation and culture of mouse PDAC spheroids

For the establishment of mouse pancreatic tumour spheroid culture, 1 × 10⁴ wild-type and COX2-KO KPC cells were resuspended in 50 µl Matrigel, plated in 4-well culture plates (Nunc) and grew in Mouse Complete Medium (Advanced DMEM/F12) supplemented with 10 mM HEPES, antibiotics (penicillin G 100 U ml−1 and streptomycin sulfate 100 U ml−1), 1% GlutaMax, B-27 supplement, 10 mM nicotinamide, 1.25 mM N–acetylcysteine, 10 ng ml−1 recombinant human R–spondin1, 100 ng ml−1 recombinant human FGF10, 100 ng ml−1 recombinant human Noggin, 500 nM A83–01, 50 ng ml−1 recombinant human EGF, 10 nM Gastrin1 and 10.5 µM Y–27632. Spheroid cultures were split at confluence by dissolving Matrigel in cold splitting medium (Advanced DMEM/F12 supplemented with 10 mM Hepes, 1% GlutaMAX and antibiotics (100 U ml−1 penicillin G and 100 U ml−1 streptomycin sulfate)). Spheroids were then mechanically disrupted with a 21G needle syringe, centrifuged for 5 min at 300g, and washed with splitting medium. After a second centrifugation, dissociated spheroids were resuspended in Matrigel and spotted as domes (50 µl per dome) in 4-well culture plates with Mouse Complete Medium. For orthotopic injections, wild-type and COX2-KO KPC-derived spheroids were collected after 6 passages in cold splitting medium and centrifuged at 300g for 5 min at 8 °C. Spheroids were then mechanically dissociated, centrifuged at 300g for 5 min, and resuspended in a solution of 25% Matrigel in PBS. Dissociated spheroids (1 × 10⁶ cells in 50 µl) were injected orthotopically in immune-competent mice as described above.

Generation and culture of mouse PDAC organoids

Mouse PDAC organoids from IL1R1 wild-type or IL1R1-KO KPC cells were generated according to previously published protocol[56]. In brief, IL1R1 wild-type or IL1R1-KO KPC cells were subcutaneously injected into C57BL/6 N mice as described above. At 11 days dpi, tumours were explanted and manually minced into 1–2 mm3 pieces in splitting medium, incubated for 1–2 h at 37 °C in pre-warmed digestion solution (splitting medium supplemented with 0.125 mg ml−1 collagenase type I, 0.125 mg ml−1 dispase II and 0.1 mg ml−1 DNase I), and further mechanically dissociated by vigorously pipetting. Dissociated samples were then filtered through a 70 μm cell strainer and washed with cold wash medium (DMEM high glucose supplemented with 1% FBS and antibiotics (100 U ml−1 penicillin G and 100 U ml−1 streptomycin sulfate)). Cells were pelleted at 300g for 5 min at 8 °C and washed twice with wash medium. Finally, tumour cells were resuspended in cold Matrigel, plated into 50 μl dome per well. After Matrigel solidification, 500 μl of warm mouse complete medium supplemented with 10.5 μM ROCK inhibitor were added to each well.

In vitro stimulation of mouse PDAC organoids

Four domes of organoids (passage 3) obtained from either IL1R1 wild-type (n = 4) or IL1R1-KO (n = 4) tumours were incubated in dispase solution (splitting medium supplemented with 2 mg ml−1 dispase II) for 20 min at 37 °C, to allow matrix dissociation. Matrix-free organoids were centrifuged at 300g for 5 min at 8 °C, and dissociated by incubation with TrypLE digestion enzyme at 37 °C for 10 min, followed by addition of Dispase Solution supplemented with 0.1 mg ml−1 DNase I for 10 min. Cells were counted and seeded at 5 × 103 single cells per well in 4 wells of 8-well glass bottom μ-Slides (Ibidi) in a final volume of 100 μl Matrigel per well. Cultures were maintained in mouse complete medium supplemented with 10.5 μM ROCK inhibitor and stimulated with 10 ng ml−1 IL-1β where indicated, replacing the medium and the stimulus every 72 h for a total of five days.

Analysis of organoid-forming efficiency

For freshly prepared organoids, the forming efficiency was assessed after 6 days of culture. Each tumour (n = 4 per group) was plated in 8 domes, and for each dome four different brightfield images were captured to allow the counting of live organoids. Then, the mean number of organoids per field, normalized for the volume of the tumour of origin, was calculated.

For organoids stimulated with IL-1β, samples were fixed for 20 min in 4% PFA at 37 °C and processed for immunofluorescence analysis. In brief, after fixation, organoid cultures were permeabilized with PBS + 0.5% Triton X-100 at 37 °C for 30 min and then incubated in blocking

buffer (PBS + 5% BSA + 10% Donkey Serum (Jackson Immunoresearch) + 0.5% Triton X-100) at 37 °C for 30 min. Samples were then incubated with Alexa Fluor 488 Phalloidin (Invitrogen A12379, 1:200) in 1% BSA for 3 h at room temperature. Nuclei were counterstained with DAPI for 10 min at room temperature. Samples were imaged on an Olympus FluoVIEW 3000 RS confocal laser scanning system using UPLXAPO 4×/0.16 objective, by acquiring 3 × 3 grids and optical sections of 33 μm each (1,95 AU) were collected for each well to cover the entire Matrigel area.

Data processing

Image segmentation was performed using the machine learning tool of the Arivis Vision 4D software (ZeissAG) using annotated ROIs as training input. Identified image objects were filtered by sphericity (>0.6) and volume (>10^3 μm^3). The volume and the number of organoids for each well were calculated and exported for statistical analyses. The same parameters for organoid identification were applied to all the imaged samples.

In vitro stimulation of tumour cells and organoids with IL-1β for gene expression analysis

KC, KPC cell lines (2D) and KPC-derived organoids (3D) were cultured as described above and stimulated with IL-1β to the final concentration of 10 ng ml−1 for the indicated time points or left untreated. At the end of the stimulation, KPC organoids were dissolved in cold Cell Recovery Solution (Gibco) at 4 °C for 20 min in agitation, centrifuged at 400g for 5 min at 4 °C, and resuspended in lysis buffer (ReliaPrep RNA Cell Miniprep System, Promega). Bulk and scRNA-seq were performed as described below.

Lentiviral transduction of KPC cells

Il1r1 cDNA was synthetized and cloned in the pCCLsin.PPT.hPGK.GFP.wpre plasmid by GenScript DNA Synthesis service. Lentiviral vectors were produced, concentrated and titrated as previously described[57]. For KPC transduction, single IL1R1-KO clones (2 × 105 cells) were transduced with a multiplicity of infection of 10. Two weeks after transduction, IL1R1+ cells were sorted (FACSAria instrument; BD Biosciences) and expanded in vitro for tumour inoculation. Polyclonal IL1R1-reconstituted pools were generated mixing an equal amount of five validated clones. The presence of the targeted protein was further validated by western blot analyses.

Flow cytometry

If not differently stated, single-cell suspensions were incubated with mouse FcγIII/II receptor (CD16/CD32) blocking antibody for 10 min on ice and pelleted by centrifugation. Cell viability was assessed by Aqua Live/Dead staining, applied for 30 min at 4 °C. Surface staining was then performed with fluorophore-conjugated primary antibodies for 30 min at 4 °C. For intracellular staining, samples were fixed with IC Fixation Buffer (Biolegend) and

permeabilized with Intracellular Staining Perm Wash Buffer 10X (Biolegend) according to manufacturer's instructions. For detection of intracellular IFNγ and TNF, tumour-draining lymph nodes were processed as described above. Single-cell suspensions were incubated in a 96-well plate with Cell Activation Cocktail with Brefeldin A (Biolegend) for 3 h at 37 °C, and then stained as described above. To assess cell apoptosis and viability, KC and KPC cells (wild-type and COX2-KO) were washed with cold PBS and resuspended in annexin V binding buffer (PE Annexin V Apoptosis Detection kit, Biolegend). Cells were stained following manufacturer's instructions. For the quantification of the intracellular IL-1β in monocytes, total bone marrow cells were seeded in a 48-well plate at a density of 2 × 106 cells per well in IMDM supplemented with 10% FBS, antibiotics (penicillin G 100 U ml−1 and streptomycin sulfate 100 U ml−1) and 2 mM l-glutamine and stimulated as indicated. After stimulation, samples were processed for flow cytometry analysis as reported. After exclusion of doublets and dead cells, monocytes were gated as CD11b+Ly6G−Ly6C+. Absolute cell count was performed using Precision Count Beads (Biolegend), following manufacturer's instructions. All samples were acquired on BD FACSymphony and FACSCanto II using DIVA software v.8.0.2 (BD Biosciences). Data were analysed with FlowJo Software (v. 10.8.1). Gating strategies of flow cytometry analysis are reported in Supplementary Fig. 2.

Cell proliferation assay

KC or KPC cells were seeded in a 96-well plate at a density of 1 × 104 cells per well in technical triplicate. After 4, 24, 48 and 72 h of culture, 10 μl per well of WST-1 reagent (Abcam) was added and cells were incubated for 30 min in standard culture conditions. After incubation, OD values (450 nm) were acquired at Multiskan GO Microplate Spectrophotometer (Thermo Scientific) and proliferation was calculated as fold change over the 4 h.

RT-qPCR

Total RNA was extracted using the ReliaPrep RNA Cell Miniprep System (Promega) and quantified with NanoDrop 8000. Single-stranded cDNA was synthesized using ImProm-II Reverse Transcription System (Promega) starting from 400-500 ng total RNA. For monocytes isolated from total bone marrow, cDNA was synthesized using SuperScript II (Thermo Scientific), amplified via PCR with KAPA HiFi HotStart (Roche) and purified with AMPure XP beads (Thermo Scientific). Sample concentration was assessed by Qubit 3.0 and size distribution by an Agilent 4200 Tapestation system. Amplification of target genes was performed with Fast SYBR Master Mix on a ViiA7 Real-Time PCR System. A complete list of primer pairs used is reported in the Supplementary Table 4.

Analyses of cell culture supernatant

Mouse BMDMs, bone marrow monocytes and tumour cells were stimulated as indicated. For quantification of IL-1β, mouse BMDMs and bone marrow monocytes were stimulated for 4 h

as indicated and ATP (5 mM) was added for the last 30 min of stimulation. Supernatants were collected and centrifuged to remove cellular debris. IL-1β (Mouse IL-1 beta Uncoated ELISA, Invitrogen) and M-CSF (DuoSet ELISA Mouse M-CSF; R&D) were measured following manufacturer's instructions. Absorbance was measured on a Multiskan GO Microplate Spectrophotometer. Other human and mouse cytokines were measured using Bio-Plex Pro Mouse Chemokine 31-Plex Assays (Bio-Rad) and Bio-Plex Pro Human Cytokine Screening Panel, 48-Plex (Bio-Rad), according to the manufacturer's indications. Acquisition was performed using Luminex instruments and analysed with Bio-plex manager (Bio-Rad) software.

PGE2 levels were quantified either in the supernatants of human tissue samples, obtained as described above, or in the supernatants of KC, KPC and Panc02 cell lines. PDAC cells were seeded at 1 × 106 cells per 10-cm dish and cultured for 24–48 h in 6 ml of complete medium. Supernatants were collected and centrifuged to remove cellular debris. PGE2 (Prostaglandin E2 Express ELISA kit, Cayman Chemical) was measured following manufacturer's instructions. Absorbance was measured on a Multiskan GO Microplate Spectrophotometer. When indicated, PGE2 levels were normalized by tissue weight.

Extraction of prostaglandins by solid phase extraction purification

Prostaglandins were extracted as previously described[58] with minor modifications. In brief, 35 mg of tissue was homogenized in 3 ml of 15% methanol in water at pH 3 (containing formic acid 0.04%) containing PGE2-d4 and PGD2-d4 (40 ng each) as internal standards and 0.005% BHT to prevent prostaglandin oxidation, using an electric pestle. The homogenate was then vortexed for 5 min and subjected to 10 min of centrifugation (2,000g) at 4 °C to remove the precipitated proteins. The supernatant was loaded onto an OASIS HLB prime vac Cartridge (3cc) and allowed to completely enter the packing material. The cartridge was washed with 3 ml 15% methanol and 3 ml water. The prostaglandins were eluted from the cartridge with 3 ml ethyl acetate containing 1% methanol. The eluted samples were dried under nitrogen and resuspended with 50 µl acetonitrile:water (1:2) and stored at −20 °C until liquid chromatography–tandem mass spectrometry (LC–MS/MS) analysis. For PGE2 and PGD2 absolute quantification, calibration curves were prepared by spiking increasing amount of PGA1 (from 0.0625 ng to 625 ng) in the same sample matrix (mouse or human control sample). The calibration curve point samples were then processed as described above, including the addition of PGE2-d4 and PGD2-d4 (40 ng each) for the extraction yield correction.

Chromatographic separation of PGE2 and PGD2 and their LC–MS/MS detection

Samples were directly analysed using the UPLC 1290 (Agilent Technologies) coupled to the TripleTOF 5600+ mass spectrometer (SCIEX) (ProMeFa, Proteomics and Metabolomics Facility, Ospedale San Raffaele, Milan, Italy). Chromatographic separations occurred on C18 column (ACQUITY UPLC HSS T3 Column, Waters, 1.8 µm, 2.1 mm × 100 mm) by directly

injecting 10 μl of samples (1/5 of the original sample). Metabolites were separated using a flow rate set at 0.4 ml min−1 and a gradient of solvent A (water, 0.1% formic acid) and solvent B (acetonitrile, 0.1% formic acid). The gradient, in negative mode, started from 25% B hold for 2 min; increased up to 40% B in 16 min; increased again up to 90% in 1 min; maintained constant at 90% B for 4 min; decreased to 25% B in 1 min and maintained at 25% for 2 min. The column was set at 50 °C while the samples were kept at 4 °C. Full scan spectra were acquired in the mass range from m/z 50 to 500. Automated calibration was performed using an external calibrant delivery system which infuses APCI negative calibration solution every 5 samples injection. A product ion experiment mode was used to monitor PGE2 and PGD2 mass (at 351.2 m/z) as well as internal standards PGE2-d4 and PGD2-d4 (355.4 m/z). PGA1 at 335.4 m/z was followed for the calibration curves. The source parameters were: gas 1: 33 psi, gas 2: 58 psi, curtain gas: 25 psi, temperature: 500 °C and ion spray voltage floating: −4,500 V, DP: −80 V, CE: 44 V.

Immunofluorescence staining

For immunofluorescence analysis of macrophage spatial distribution, tissues were fixed overnight in 4% paraformaldehyde at 4 °C, washed in PBS and placed in 30% sucrose for 12–24 h. Afterwards, tissues were placed in a 2:1 mixture of 30% sucrose and optical cutting temperature (OCT) compound (Bio Optica, 05-9801) for 30 min at 4 °C, embedded in OCT and snap frozen in dry ice. The 10-μm cryostat sections were fixed in paraformaldehyde (4% in PBS) at room temperature for 20 min, washed 3 times in 0.05% PBS-Tween (PBS-T) and incubated with blocking buffer (0.05% PBS-T + 0.3% Triton X-100 + 5% BSA) at room temperature for 1 h. Sections were stained overnight at 4 °C with the following primary antibodies: rat anti-mouse F4/80 (Abcam ab6640, 1:200) or rabbit anti-mouse F4/80 (Abcam ab30042, 1:500), goat anti-mouse IL-1β (R&D Systems AF-401-NA, 1:100), rat anti-mouse FOLR2 (BioLegend 153302, 1:100), rabbit anti-mouse KRT19 (Abcam ab52625, 1:500), goat anti-mouse CD31 (R&D Systems AF3628, 1:500), rat anti-mouse VEGFR2 (BD Pharmingen 550549, 1:100) or rabbit anti-mouse PDGFRα (Abcam ab203491, 1:500). Sections were washed three times in 0.05% PBS-T, and incubated with the following secondary antibodies: donkey anti-rat IgG Alexa Fluor Plus 488 (Invitrogen A48269, 1:500), donkey anti-goat IgG Alexa Fluor Plus 555 (Invitrogen A32816, 1:500), donkey anti-rabbit IgG Alexa Fluor Plus 647 (Invitrogen A32795, 1:500). After three washes in 0.05% PBS-T, cell nuclei were stained with DAPI (Sigma-Aldrich Merck, MBD0015) at room temperature for 15 min and coverslips were mounted onto slides with FluorSave Reagent (Sigma-Aldrich Merck, 345789). Digital images were acquired on a MAVIG RS-G4 scanning confocal microscope (Caliber I.D.) using a 20× air objective or a 40× oil objective.

Immunofluorescence analysis of macrophage spatial distribution

Quantitative analysis of immunofluorescence images was performed using QuPath v0.4.159. For each image, tissue-specific expression of cytokeratin 19 (KRT19) was used to annotate tumour areas and discriminate them from the adjacent stroma. Equally sized ROIs were randomly selected within the annotated 'tumour' (DAPI+KRT19+) or 'stromal' (DAPI+KRT19−)

areas. Within each ROI, cell segmentation was performed using the 'cell detection' command based on the nuclear DAPI stain and thresholds were applied on fluorescence signals to create classifiers for cell-type identification. Specifically, F4/80 signal was used to classify cells as macrophages and compute their abundance in annotated ROIs. Similarly, the macrophage classifier was combined with classifiers based on IL-1β and FOLR2 signals to detect double-positive cells. Quantification was performed by computing the frequency of F4/80+, F4/80+IL-1β+ and F4/80+FOLR2+ cells in n = 10–20 ROIs per tissue section, equally distributed between tumour and stromal compartments. Additionally, the frequency of macrophages was quantified in normal adjacent tissue from orthotopic PDAC mice and in healthy pancreas from wild-type controls. For distance analysis, the frequency of F4/80+IL-1β+ and F4/80+FOLR2+ macrophages was calculated within concentric partitioning rings annotated around the tumour margin (identified by KRT19 staining), with a cumulative 50-µm expansion in the adjacent stroma. The same parameters for segmentation and cell-type classification were applied to all samples from the same experiment.

Immunofluorescence analysis of IL-1β+ TAMs in areas of angiogenesis

Quantitative analysis of IL-1β+ TAMs in areas of angiogenesis was carried out with QuPath v0.4.1. Cell segmentation was performed on whole-tissue sections (comprising tumour and stroma) using the 'Cell detection' command based on the nuclear DAPI stain and object classifiers were set up to detect CD31+VEGFR2+ endothelial cells. The 'Density map' command was then used to split the tissue section into areas with 'high' and 'low' density of CD31+VEGFR2+ endothelial cells, and quantify the frequency of F4/80+IL-1β+ cells within these discrete tissue annotations.

Immunofluorescence analysis of IL-1β+ TAMs in areas of hypoxia

Tumour hypoxia was labelled in vivo with Hypoxyprobe, following the manufacturer's instructions. In brief, pimonidazole (Hypoxyprobe-1, 60 mg kg−1 of body weight) was intraperitoneally injected in end-stage orthotopic KPC-bearing mice 60 min before euthanasia. Fresh tumour biopsies were washed in PBS, embedded in OCT compound and snap frozen in dry ice. Ten-micrometre cryostat sections were processed for immunofluorescence staining as described above, using the following primary antibodies: rat anti-mouse F4/80 (Abcam ab6640, 1:200), rabbit anti-mouse KRT19 (Abcam ab52625, 1:500), goat anti-mouse IL-1β (R&D Systems AF-401-NA, 1:100), anti-pimonidazole (Hypoxyprobe PAb2627AP, 1:20). Digital images were acquired on a MAVIG RS-G4 scanning confocal microscope (Caliber I.D.) using a 20× air objective. Quantitative analysis was carried out with QuPath v0.4.1, by performing DAPI-based cell segmentation of the whole tumour and stroma and using the 'Density map' command to define annotations comprising areas with high density of cells stained for Hypoxyprobe. The ensuing density maps were then used to annotate tissue regions as 'hypoxic' or 'non-hypoxic' and quantify the frequency of F4/80+ IL-1β+ cells within these compartments.

Immunohistochemistry staining of human PDAC

Immunohistochemistry staining of human PDAC tissue was performed using the Discovery Ultra (Roche/Ventana) platform. In brief, 5-μm tissue sections collected from FFPE blocks of human PDAC were deparaffinized, subjected to antigen retrieval with Discovery CC1 solution (Roche/Ventana, 950-500) for 60 min and blocked with Discovery Inhibitor (Roche/Ventana, 760-4840) for 8 min. Tissue sections were sequentially stained for 30 min at room temperature with the following primary antibodies: rabbit anti-human NLRP3 (Sigma-Aldrich Merck HPA012878; 1:150), mouse anti-human CD163 (MRQ-26, Cell Marque 163M-18, pre-diluted), mouse anti-human FOLR2 (Invitrogen MA5-26933, 1:100), mouse anti-human cytokeratin 8 and 18 (B22.1 and B23.1, Cell Marque 818M-90, pre-diluted). For each staining cycle, incubation with primary antibody was followed by incubation with Discovery UltraMap anti-Ms HRP (Roche/Ventana, 760-4313) or Discovery UltraMap anti-Rb HRP (Roche/Ventana, 760-4315) for 20 min at room temperature, and then with one of the following fluorophores at 1:100 dilution for 4-8 min at room temperature: Discovery FITC kit (Roche/Ventana, 760-232), Discovery Red 610 kit (Roche/Ventana, 760-245), Discovery Cy5 (Roche/Ventana, 760-238). Tissue sections were neutralized with Discovery Inhibitor at the end of each staining cycle to avoid cross-reactivity. Finally, tissue sections were counterstained with DAPI and coverslips were mounted onto slides using Vectashield Antifade Mounting Medium (Vector Laboratories, H-1000-10). Digital images were acquired on a MAVIG RS-G4 scanning confocal microscope (Caliber I.D.) using a 20× air objective.

Western blot analyses

Cells were lysed in RIPA lysis buffer, containing 10 mM Tris-HCl pH 8, 1 mM EDTA pH 8, 140 mM NaCl, 1% Triton X-100, 0.1% SDS, 0.1% deoxycholate and protease and phosphatase inhibitors. Protein concentrations were measured with the Pierce BCA Protein Assay Kit. Lysates were then electrophoresed on Tris-glycine SDS–PAGE gels and transferred on nitrocellulose membranes (Amersham Protran Premium 0.45 μm NC). Membranes were blocked in PBS-T buffer added with 5% BSA or 5% milk (1 h at room temperature), followed by overnight incubation with primary antibodies at 4 °C: anti-IκBα (9242 S, Cell Signaling, 1:1,000), anti-IL1R1 (ab229051, Abcam, 1:1,000) and anti-COX2 (160106, Cayman Chemical, 1:100). The following day, membranes were washed and incubated for 1 h at room temperature with HRP-conjugated secondary antibody. Membranes were developed either with Clarity Western ECL Substrate (Bio-Rad) or Westar Supernova (Cyanagen). Protein loading was assessed by detection with anti-β-actin (A1978, Sigma-Aldrich, 1:2,000) or anti-vinculin (13901 S, Cell Signaling, 1:1,000). Western blot analyses were performed using Image Lab Software v6.1. Uncropped and unprocessed scans of western blots are reported in Supplementary Fig. 1.

Generation and processing of scRNA-seq data

Data generation

Human and mouse samples were collected and dissociated as described above. For the patient LiMeT PDAC15, cells were enriched in the myeloid fraction as CD45+CD3−CD19− by sorting (FACSAria, BD Biosciences). For heterotopic and orthotopic KC tumours, cells were enriched in the myeloid fraction as CD45+Cd11b+ via sorting and scRNA-seq libraries generated using the Chromium Single Cell 3' Reagent Kit v2, according to the manufacturers' instructions. For mouse KPC organoids, Matrigel domes containing the organoids were dissolved in Cell Recovery Solution (Gibco) for 30 min on ice, manually inverting the tubes every 5 min. After addition of cold splitting medium, organoid suspension was centrifuged and supernatant was removed prior to incubation in TrypLE Express (Gibco) for 20 min on an orbital shaker at 37 °C. The larger cellular aggregates were allowed to settle by gravity, and the single-cell suspension was collected from the supernatant without interfering with the lower fraction. Upon centrifugation at 400g for 5 min at 4 °C, cells were resuspended in ultrapure BSA (400 µg ml−1) (Invitrogen) for downstream processing.

Unless otherwise stated, scRNA-seq libraries were generated using a microfluidics-based approach on Chromium Single-Cell Controller (10X Genomics) using the Chromium Single Cell 3' Reagent Kit v3.1, according to the manufacturers' instructions. In brief, single cells were partitioned in gel beads in emulsion (GEMs) and lysed, followed by RNA barcoding, reverse transcription and PCR amplification (13–15 cycles). The concentration of the scRNA-seq libraries was determined using Qubit 3.0 and size distribution was assessed using an Agilent 4200 TapeStation system. Libraries were sequenced on an Illumina NovaSeq 6000 instrument (paired-end, 150 bp read length).

Data processing

Fastq files were processed with Cell Ranger (v 4.0.0)[60], using default parameters. Reads were aligned to reference genome mm10 for mouse samples and hg38 for human samples (references version 2020-A, 10X Genomics). Only confidently mapped reads with valid barcodes and unique molecular identifiers (UMIs) were retained to compute a gene expression matrix containing the number of UMI for every cell and gene. Gene counts were imported in R environment (v 4.0.3) and processed with Seurat (v 4.0.3). When creating the Seurat object, genes expressed in less than 3 cells were removed. Putative doublets were identified and discarded using scDblFinder R package (v 1.4.0)[61] by imputing doublet rates (dbr) equal to 0.07 for mouse sample and 0.05 for human samples. Dbr were established in agreement with the number of loaded cells and following the 10X Genomics guidelines. Cells expressing less than 1,000 UMI counts were discarded. Cells expressing less than 200 genes (mouse sample), or less than 500 genes (human sample) were also excluded. Lastly, cells with a ratio of mitochondrial versus endogenous genes expression exceeding 0.25 (mouse sample) or 0.40 (human sample) were discarded. Raw expression data were normalized applying log2 transformation with NormalizeData function, scaled using ScaleData function, regressing on percentage of mitochondrial gene expression and cell cycle scores, previously computed using CellCycleScoring function. The top 3,000 genes with the highest standardized variance were computed using FindVariableFeatures function

(selection.method = "vst"). Principal component analysis (PCA) was computed using RunPCA function with default parameters.

Batch correction

PCA embeddings were corrected for sample batch by applying alternative algorithms to the same Seurat object through the Seurat Wrapper package (v 0.3.0). For both human and mouse data, when analysing the whole or tumour cells dataset, batch effect was corrected employing matching mutual nearest neighbour (MNN) algorithm[62], implemented by RunFastMNN function using default parameters. For the analysis of mononuclear phagocytes and TAMs, batch correction was achieved with the Harmony algorithm (v 0.1.0)[63], implemented by RunHarmony function using the first 30 PCA dimensions and default theta (theta = 3 for human dataset).

Graph-based clustering and differential gene expression analyses

Shared nearest neighbour (SNN) graph was computed using the FindNeighbors function, taking as input the first 20 PCA dimensions. Cell clusters were defined using Louvain algorithm with the FindCluster function. For visualization in two dimensions uniform manifold approximation and projection (UMAP)[64] was used. Cluster-specific genes were identified using FindAllMarkers function with option only.pos = TRUE and min.pct = 0.1, setting a cut-off of FDR < 0.01.

Inference of copy number variants

Single-cell copy number variants were inferred using CopyKAT R package (v 1.0.5)[65]. CopyKAT estimates the genome copy number profile of single cells employing an integrative Bayesian segmentation approach combined with hierarchical clustering to identify putative aneuploid cells. CopyKAT was run separately on each human sample, taking the raw count matrix of all cells as input and adjusting the segmentation parameter KS.cut to either 0.1 or 0.15 according to data quality.

Human–mouse comparison of TAM clusters

We performed a pre-ranked GSEA analysis with clusterProfiler R package (v 3.18.1)[66] on mouse TAM genes ranked by log2FC (each TAM subset vs other TAMs) using as gene sets mouse orthologues of human TAMs marker genes obtained using biomaRt (v 2.46.3)[67] database. To identify shared signatures for each human and mouse TAM cluster, we computed overlaps between marker genes identified using logfc.threshold = 0.8.

RNA velocity and single-cell trajectories

Mouse classical monocytes and TAMs from pancreatic and blood samples were analysed together as previously described. Batch effect correction was performed by MNN algorithm[62], using the RunFastMNN function with default parameters. The first 20 MNN-corrected principal components were used to compute the two-dimensional embedding using the diffusion map-based algorithm Palantir[68], implemented with the RunPalantirDiffusionMap function from SeuratExtend R package (v 0.4.2). Cell clusters were defined according to marker-based manual annotation previously done on each dataset. The Seurat object was then converted into Scanpy format (v 1.6.0)[69] using SeuratDisk (v 0.0.0.9019) and the following analyses were performed in Python environment (v 3.6.10). To annotate spliced and unspliced reads, cell-barcode sorted bam files from Cell Ranger output were processed using Velocyto pipeline (v 0.17.17)[70]. The scVelo Python package (v 0.2.2)[71] was used to compute RNA velocity vectors for each gene, employing dynamical modelling to estimate splicing kinetics. Using CellRank package (v 1.2.0)[20], RNA velocity and transcriptomic similarity information were combined in single kernel to compute a cell-cell transition matrix. Generalized Perron cluster cluster analysis (GPCCA) estimator[72] was used to identify macrostates. Terminal states were inferred by inspecting the coarse-grained transition matrix and were then used to compute absorption probabilities. Focusing on the classical monocyte–Il1b+ TAM lineage, genes whose expression correlates with absorption probabilities towards Il1b+ TAMs terminal state were identified as potential lineage drivers.

Optimal transport analysis

To infer cell trajectories, we applied Waddington optimal transport[19] on our scRNA-seq mouse time-course data. Optimal transport model was fit to classical monocytes and TAMs from pancreatic and blood samples, setting $\varepsilon = 0.05$, $\lambda1 = 1$ and $\lambda2 = 50$ to compute transport maps. Based on them, we computed cell fate probabilities using cell populations at day 30 as endpoint.

Gene set enrichment analysis

Hallmarks gene sets were retrieved from msigdbr (v 7.5.1)[73]. For GO biological processes gene sets, we used org.Hs.eg.db (v 3.12.0) and org.Mm.eg.db (v 3.12.0) as genome wide annotations for human and mouse respectively. Gene sets of cytokine-induced signatures were derived from in vitro stimulation experiments on mouse bone marrow-derived macrophages[22,25] (Supplementary Table 4).

IL1B gene expression in human cell types

To evaluate the expression of IL1B across all human cell types, we reanalysed scRNA-seq data including neutrophils in the dataset. Neutrophils were retrieved lowering the cut-offs on UMI counts and genes per cell to 500 and 100, respectively. Data were processed as previously

described, with the exception that counts were normalized with SCTransform function in Seurat.

Re-analysis of human PDAC cells in naive samples

Tumour cells from untreated participants were analysed separately as previously described. We computed new embedding and clustering on cells showing variable expression of the T1RS signature (clusters 1,3,5 at resolution 0.3) and then we performed trajectory analysis with slingshot31 (v. 1.8.0) on the MNN space. We correlated gene expression with pseudotime, computed with slingPseudotime function. To evaluate if cell trajectory reflected the acquisition of the expression of T1RS signature we performed GSEA analyses on gene list ranked by correlation values. Finally, to define which ligand–receptor interaction in the crosstalk between IL1B+ TAMs and tumour cells drives the acquisition of the T1RS gene expression pattern through the trajectory, we performed a cell-cell communication analysis with NicheNet32 (v. 1.1.1). We interrogated NicheNet database using IL1B+ TAMs as sender cells and tumour cells as receiver cells. Putative ligands were selected filtering for genes expressed in IL1B+ TAMs subset (percentage of cells > 15% and log2FC(IL1B+ TAMs/other TAMs) > 0.5), while putative receptors were selected filtering for genes expressed in the tumour cells (percentage of cells > 15% in clusters 1,3 and 5). We used markers of the cluster at the endpoint of the trajectory (log2FC > 1 and min.pct = 30%) as target genes for ligand prioritization.

scRNA-seq datasets collected in this study

We collected published scRNA-seq data on human PDAC and normal adjacent tissue (CRA001160)27; immune cells from idiopathic or hereditary pancreatitis and normal pancreas (GSE165045)30; pancreatic epithelial cells from GEMMs of PDAC progression (GSE207943)28. For these datasets we downloaded: raw fastqs, raw count matrices and normalized counts, respectively. Data were processed as previously described.

scRNA-seq dataset from patients with pancreatitis

Raw counts matrices of immune cells from idiopathic or hereditary pancreatitis and normal pancreata were filtered to discard cells expressing less than 200 genes, less than 1,000 UMIs and with a ratio of mitochondrial versus endogenous genes expression exceeding 0.20. Cells were processed as previously described, using 2,000 variable features. For the analysis of macrophages, anchoring-based transfer learning74 was used to perform annotation, using our TAM dataset as reference. Anchors for transfer learning were computed using the FindTransferAnchors Seurat function. Reference labels were then projected onto query macrophages using the TransferData function. Macrophages from pancreatitis and donor pancreata were annotated according to our reference classification if the prediction score exceeded 0.75, otherwise were left unlabelled.

scRNA-seq datasets from other mouse models

scRNA-seq datasets from GEMM mouse models and wild-type and COX2-KO KPC were processed as previously described. For scRNA-seq data derived from heterotopic and orthotopic KC tumours we corrected batch effect employing Harmony algorithm (v 0.1.0)[63], implemented by RunHarmony function using the first 30 PCA dimensions and theta = 1. For the reclustering of mononuclear phagocytes, batch correction was achieved with the Harmony algorithm (v 0.1.0) on the first 30 PCA dimensions and default theta. Differentially expressed genes in the comparison between cells from wild-type and COX2-KO tumours were computed using FindAllMarkers function with option only.pos = FALSE, min.pct = 0.1, setting a cut-off of FDR < 0.01 and average log2FC > 0.5.

Generation and processing of spatial transcriptomic data

Visium spatial gene expression

Data generation

Spatial transcriptomics data were generated using the Visium Spatial Gene Expression Reagent Kits (10X Genomics) according to the manufacturer's instruction. Tumour biopsies from day 30 orthotopic PDAC mice were gently washed in PBS, snap frozen via bathing in liquid nitrogen-chilled isopentane and embedded in OCT compound. Five to ten sections were collected to evaluate RNA quality at TapeStation system (Agilent). The tissue blocks were then processed to retrieve 2 non-sequential 10 µm sections (100 µm apart), which were placed within the 6.5 × 6.5 mm capture areas of a Visium slide equilibrated at cryostat temperature (−20 °C). Sections were immediately fixed in chilled methanol at −20 °C for 30 min and stained via immunofluorescence using buffers supplemented with Recombinant RNase inhibitor (Takara 2313 A, 2 U µl−1) to prevent RNA degradation. Whole-slide images were acquired using the MAVIG RS-G4 (Caliber I.D.) confocal microscope at 20× magnification. Barcoded libraries were generated by permeabilizing tissue sections at 37 °C for 15 min and performing in situ reverse transcription at 53 °C for 45 min, followed by second-strand synthesis at 65 °C for 15 min. cDNA was denatured and transferred to tubes for PCR amplification and library construction, including fragmentation, adapter ligation and sample indexing. The quality of both amplified cDNA and final libraries was determined at TapeStation system (Agilent). Visium libraries were sequenced on an Illumina NovaSeq 6000 instrument (paired-end, 150 bp read length).

Data processing

Spatial transcriptomic data were aligned to their corresponding immunofluorescence image, using SpaceRanger (v 1.2.0) with default parameters. We excluded spots with a number of UMI lower than 100 and without DAPI staining in the corresponding overlaid image, resulting in a dataset of 3,274 and 3,496 spots for A1 and B1 sections, respectively. To infer cell-type proportions within each spot, we performed cell-type deconvolution using DestVI (v 0.1)[75]. We first trained the single-cell latent variable model (scLVM) on the scRNA-seq dataset

obtained by retaining transcriptomic data from samples collected 30 days post-tumour inoculation, analysed and annotated as described previously. We then trained the spatial transcriptomic latent variable model on the spatial transcriptomic dataset and we computed cell-type proportions for each spot with get_proportions() function. To assess spatial variability of macrophage transcriptome, spatial transcriptome spots enriched in monocytes and macrophages were selected using the default secondary cut-off, set by DestVI on their proportion distributions, obtaining a dataset of 671 spots for A1 and 1,119 spots for B1. We computed the gamma latent space with get_gamma() function, obtaining 5 gamma values, and the Spatial Principal Components (Spatial PCs) using the get_spatial_components() function. Finally, gene expression values were imputed using get_scale_for_ct() function, extracting six different gene expression matrices from the negative binomial distribution, as predicted by the trained scLVM applied to spatial transcriptome latent space. The mean gene expression values computed on these expression matrices were used for downstream analysis. Spot enrichments for specific gene sets were evaluated using runPAGEEnrich() function from Giotto R package (v 1.1.2)[76]. For A1 spatial transcriptome dataset, we performed clustering analysis with Seurat package (v 4.2.0): spot read counts were normalized with SCTransform() function and PCA performed with RunPCA() function. Top 20 PCs were used to obtain clusters at 0.3 resolution using FindNeighbors() and FindClusters() functions. Marker genes of spots belonging to cluster 4 or cluster 6 were ranked by log2FC and used to perform GSEA analysis for selected GO Biological Processes.

Annotation of spatial transcriptome spots

Single-channel grayscale immunofluorescence images for sections A1 and B1 were imported in CellProfiler (v. 4.1.3)[77], rescaled using RescaleIntensity() function, and imported as composite images in Squidpy (v 1.2.3)[78]. DAPI-based cell nuclei detection was carried out with Stardist (v 0.8.3)using the pre-trained 2D versatile algorithm for fluorescence data, to create mask binary files. In parallel, single-channel image crops were generated for every spatial transcriptome spot. Resulting images and masks were exported to Cell Profiler, where nuclei were filtered based on size and cell boundaries were reconstructed using the 'distance' option. A median filter was applied to F4/80, PDGFRa and KRT19 signal intensity to classify cells as positive or negative for each individual marker. Results were exported to R, double- and triple- positive cells were filtered out, and the fraction of single F4/80+, PDGFRa+ or KRT19+ cells was calculated for all the spots. Finally, spatial transcriptome spots were annotated as 'tumour' or 'stroma', according to transcript or protein expression obtained from spatial transcriptome or immunofluorescence data, respectively. For immunofluorescence-based annotation, the percentage of KRT19+ cells as calculated by CellProfiler was used to classify spots as tumour (per cent of KRT19+ ≥ 60%) or stroma (per cent of KRT19+ < 60%). For spatial transcriptome-based annotation, DestVI deconvolution output was used to define tumour spots as those where the sum of percentages of cancer, ductal and acinar cells was ≥60%. Similarly, stromal spots were defined as those where the sum of endothelial cells and cancer-associated fibroblasts was ≥40%. Spots that did not fall in these two categories, were annotated as tumour or stroma according to the most enriched cell type.

Molecular Cartography

Data generation

Ten-micrometre sections were collected from fresh frozen PDAC tissues, placed within the capture areas of cold slides, and sent to Resolve Biosciences on dry ice for sample processing. Upon arrival, tissue sections were thawed, fixed with 4% Formaldehyde (Sigma-Aldrich F8775) in PBS for 20 min at 4 °C, and used for Molecular Cartography (100-plex combinatorial single molecule fluorescence in situ hybridization) according to the manufacturer's instructions (protocol 1.3; available for download from Resolve's website for registered users). In brief, tissue sections were hybridized at 37 °C for 24 h with oligonucleotides probes specific for the selected target genes (see Supplementary Table 9). Probes were designed using Resolve's proprietary algorithm, as previously reported[79]. Afterwards, probe binding was revealed with fluorescent tags in a multi-step automated imaging process, repeating colour development, imaging and decolorization for a total of 8 cycles on a Zeiss Celldiscoverer 7 instrument, using a 50× water immersion objective. The resulting raw data images were pre-processed for background correction, aligned to perform spot segmentation, analysed to decode the resulting signals and to finally assign each detected transcript to xyz coordinates, as previously reported[79].

Cell segmentation

We segmented cell nuclei in the DAPI image with Cellpose[80] (v. 2.2) using the pre-trained nuclei model, with automated estimation of diameter parameter. Subsequently, cells were segmented on transcript coordinates with Baysor[81] (v. 0.5.0) using DAPI segments as prior with the following parameters:–n-clusters 1–prior-segmentation-confidence 0.2 -m 3. Finally, we computed cells outlines by applying the convex hull algorithm, using chull R function, on transcripts assigned to each individual cell by Baysor.

Cell filtering and annotation

We imported Baysor output files and segmentation into a Seurat object with a custom function. Cells expressing less than 4 genes or more then 25 genes, along with cells with less than 10 transcripts were discarded. Gene counts were normalized with SCTransform Seurat function with clip.range set form −10 to 10. Then, we performed PCA and we computed clustering and dimensionality reduction as previously described for scRNA-seq data. Finally, we computed markers for all cluster and annotated cell types.

Spatial neighbourhood analysis

For each cluster we defined a set of cells in its spatial neighbourhood, then we computed which clusters were significatively over-represented in this neighbourhood set. In brief, for each cell we computed k-nearest neighbours within spatial coordinates space using kNN function from dbscan R package[82] (v. 1.1-11), with k set to 40 and maximum distance set to

400 pixels. We selected the set of nearest neighbours of all cells belonging to the same cluster and we counted the number of cells from all different cluster within this set of nearest neighbours. We then computed significance using randomly annotated data as null distribution. Specifically, we reannotated cells randomly 1,000 times, maintaining cluster dimensionality and, for each randomization, we computed again the number of cells from all clusters in the set of nearest neighbours of each cluster.

Spatial correlation of gene expression

We computed gene expression spatial correlation of all genes with CXCL1. First, we computed the spatial lag expression vector of CXCL183. Lag expression vector of a gene reports for each cell the summed expression of its k-nearest neighbours. In brief, we used lag.listw from spded R package (v. 1.2-8) to compute the spatial lag vector for CXCL1, considering for each cell its 20 nearest neighbours, with maximum distance set to 400 pixels, defined with the kNN function. We then correlated the real expression of each gene with the spatial lag vector of CXCL1. Genes that show high spatial correlation with CXCL1 are those genes that are more expressed in cells that are close to cells expressing CXCL1 at highest level.

Spatial transcriptomic datasets collected in this study

We downloaded raw count matrices of published GeoMX data84 (GSE226829). We performed normalization with voom function of limma R package85 (v. 3.46.0).

Generation and processing of bulk RNA-seq data

Data generation

Total RNA was purified using the ReliaPrep RNA Cell Miniprep System and RNA-seq libraries were generated using the Smart-seq2 method86 with minor modification. In brief, 5 ng of RNA were retrotranscribed, cDNA was PCR-amplified (15 cycles) and purified with AMPure XP beads. After purification, the concentration was determined using Qubit 3.0 and size distribution was assessed using Agilent 4200 TapeStation system. Then, the tagmentation reaction was performed starting from 0.5 ng of cDNA for 30 min at 55 °C and the enrichment PCR was carried out using 12 cycles. Libraries were then purified with AMPure XP beads, quantified using Qubit 3.0, assessed for fragment size distribution on an Agilent 4200 TapeStation system. Sequencing was performed on an Illumina NovaSeq6000 (single-end, 75 bp read length) following manufacturer's instruction.

Data processing

Reads were aligned to the mm10 reference genome using STAR aligner (v STAR_2.5.3a)87. Read counts matrices were computed using the featureCounts function from Rsubread

package (v 2.0.1)88, using RefSeq Mus musculus transcriptome (mm10) annotation89, setting minMQS option to 255. Further analyses were performed in R environment (v 3.6.3) with edgeR R package (v 3.28.1)90. Expressed genes read counts were normalized using the calcNormFactors function, with the trimmed mean of M-values (TMM) method91. The estimateDisp function was used to estimate dispersion. Differential gene expression across conditions was computed by fitting a negative binomial generalized linear model, with the glmQLFit function, followed by a quasi-likelihood F-test, with the glmQLFTest function, including sample replicates as covariates in the design matrix. Reads per kilo base per million (RPKM) values were computed for each gene with the rpkm function.

Definition of TNF-plus-PGE2 synergized genes

RNA-seq data were generated and pre-processed as described above. Genes not passing the expression cut-off of RPKM > 1 in at least two samples in the dataset were filtered out. For each timepoint we defined TNF-PGE2-inducible genes comparing expression levels in the TNF + PGE2 condition versus untreated, PGE2 alone or TNF-alone conditions, setting log2FC(RPKM) ≥ 1.5 and FDR < 0.01 as cut-offs. We also filtered out genes not reaching RPKM > 1.5 in at least 2 samples within each comparison. Finally, for each timepoint, we defined PGE2–TNF synergized genes selecting genes passing previously defined cut-offs in all tested comparisons. For GSEA analysis we considered genes defined as PGE2–TNF synergized in at least one timepoint.

Definition of T1RS gene signature

We analysed bulk and single-cell RNA-seq data on KC, KPC cells and KPC organoids stimulated with IL-1β in vitro. For each timepoint of stimulation, we defined IL-1β-inducible genes comparing expression levels in the IL-1β condition versus untreated, setting log2FC(RPKM) ≥ 1 and FDR < 0.05 as cut-offs. For each experimental condition we defined lists of IL-1β-inducible genes, selecting genes passing the defined cut-offs in at least one timepoint. Intersection of these gene lists led us to the identification of a set of genes commonly induced by IL-1β in all experimental conditions, namely the T1RS signature.

RNA-seq datasets collected in this study

We collected published RNA-seq data on pancreatic epithelial cells from Kras-wild-type and mutant Kras mice treated either with caerulein, IL-33 or left untreated (GSE132326, GSE154543)15; mouse pancreatic spheroids derived from pancreas either pre-exposed or not exposed to inflammation (GSE180211)15. For these datasets raw count matrices were downloaded and analysed as previously described. In addition, we collected published RNA-seq data of monocytes isolated from peripheral blood of patients with PDAC and healthy donors (E-MTAB-11190)17. For these data, fastq files were downloaded and processed as previously described, using hg38 as reference genome (reference version 2020-A, 10X Genomics).

TCGA data analyses

Using the TCGAbiolinks R package (v 2.23.2)[92], we downloaded transcriptomic data and clinical data from the pancreatic adenocarcinoma (PAAD) cohort for pancreatic cancer (n = 178). Survival analysis on primary tumour samples was performed using the survival (v 3.2-10) and survminer (v 0.4.9) R packages.

Survival analysis of TAM markers and T1RS genes in the PAAD cohort

To evaluate the prognostic significance of TAM marker genes, we obtained TAM cluster-specific genes by performing differential gene expression analysis (each TAM cluster vs other TAM clusters) and filtering for log2FC ≥ 1. On such gene lists, we evaluated MNP specificity by differential gene expression analysis, selecting genes with log2FC ≥ 2 in MNP compared to other cell types identified in our scRNA-seq data. The effect on patient prognosis was assessed by Cox beta regression coefficient on genes for which the fit was significant according to Wald test P values corrected for multiple testing. Univariate Cox regression model was fit for the expression of each gene or for the expression of each gene normalized for CD68 expression as continuous variables, for the evaluation of T1RS signature or TAM marker genes respectively.

Survival analysis on the IL1B+ TAM gene signature

The six-gene prognostic signature for IL1B+ TAMs, obtained as previously described, was used to stratified patients for survival analysis. The mean expression of the signature, normalized by CD68 expression, was used to group samples into high and low groups according to the upper and the lower quartile respectively. Cox regression model was fit to compare the high group against the low group, extracting the hazard ratio and its associated P value.

Association of T1RS and IL1B+ TAM signatures

Using the TCGAbiolinks R package (v 2.28.3), we downloaded transcriptomic data and clinical data from the aforementioned cohort. We grouped patients based on the mean expression of the six-gene IL1B+ TAM signature normalized by CD68 expression into high, intermediate and low groups according to the upper and the lower quartile of the score distribution. To examine association between IL1B+ TAMs and T1RS signature, we then computed the mean of log2-transformed expression values of T1RS signature genes for each group of patients.

Cell-type deconvolution of TCGA PDAC samples

To estimate macrophage proportion in TCGA samples we used CIBERSORTx[93] online tool to deconvolute cell fractions using our annotated scRNA-seq human PDAC dataset as reference. To build the signature matrix file, we first down-sampled our scRNA-seq human

PDAC dataset, randomly selecting 200 cells for each annotated cell type. We then ran CIBERSORTx to generate cell-type signature matrices and impute the relative cell fractions in each tumour sample, enabling S-mode batch correction.

Quantification and statistical analyses

Results are illustrated as mean ± s.d. or mean ± s.e.m. Graphs show data from at least two independent repeats. Significance was defined as $P < 0.05$. Statistical analysis was conducted either using GraphPad Prism v9.0 (GraphPad Software) or R v3.4.1 (R project). Statistical tests, exact value of n and what n represents are mentioned in the figure legends. Statistical tests with adjustment for multiple comparisons and exact P values are reported in the Source Data.

Reporting summary

Further information on research design is available in the Nature Portfolio Reporting Summary linked to this article.

Data availability

Single-cell, spatial transcriptomic and bulk RNA-seq data have been deposited at NCBI GEO data repository under accession number GSE217847. Data reanalysed for this study are available under the following accession codes: CRA001160 (scRNA-seq of human PDAC and NAT), GSE165045 (scRNA-seq of patients with pancreatitis), GSE207943 (scRNA-seq of mouse PDAC GEMM), GSE226829 (GeoMX data of human PDAC), GSE132326 and GSE154543 (RNA-seq of epithelial cells from mouse PDAC), GSE180211 (RNA-seq of pancreatic spheroids), and E-MTAB-11190 (RNA-seq of blood monocytes from patients with PDAC). Source data are provided with this paper.

Code availability

Codes used for the analyses is available at https://github.com/ostunilab/PDAC_Nature_2023.

References

1. Halbrook, C. J., Lyssiotis, C. A., Pasca di Magliano, M. & Maitra, A. Pancreatic cancer: advances and challenges. Cell 186, 1729–1754 (2023).

2. Mantovani, A., Allavena, P., Marchesi, F. & Garlanda, C. Macrophages as tools and targets in cancer therapy. Nat. Rev. Drug. Discov. 21, 799–820 (2022).

3. Glass, C. K. & Natoli, G. Molecular control of activation and priming in macrophages. Nat. Immunol. 17, 26–33 (2016).

4. Amit, I., Winter, D. R. & Jung, S. The role of the local environment and epigenetics in shaping macrophage identity and their effect on tissue homeostasis. Nat. Immunol. 17, 18–25 (2016).

5. Salmon, H., Remark, R., Gnjatic, S. & Merad, M. Host tissue determinants of tumour immunity. Nat. Rev. Cancer 19, 215–227 (2019).

6. Medzhitov, R. The spectrum of inflammatory responses. Science 374, 1070–1075 (2021).

7. Mulder, K. et al. Cross-tissue single-cell landscape of human monocytes and macrophages in health and disease. Immunity 54, 1883–1900.e1885 (2021).

8. Cheng, S. et al. A pan-cancer single-cell transcriptional atlas of tumor infiltrating myeloid cells. Cell 184, 792–809.e723 (2021).

9. Bill, R. et al. CXCL9:SPP1 macrophage polarity identifies a network of cellular programs that control human cancers. Science 381, 515–524 (2023).

10. Liudahl, S. M. et al. Leukocyte heterogeneity in pancreatic ductal adenocarcinoma: phenotypic and spatial features associated with clinical outcome. Cancer Discov. 11, 2014–2031 (2021).

11. Baer, J. M. et al. Fibrosis induced by resident macrophages has divergent roles in pancreas inflammatory injury and PDAC. Nat. Immunol. 24, 1443–1457 (2023).

12. Zhu, Y. et al. Tissue-resident macrophages in pancreatic ductal adenocarcinoma originate from embryonic hematopoiesis and promote tumor progression. Immunity 47, 597 (2017).

13. Weeden, C. E., Hill, W., Lim, E. L., Gronroos, E. & Swanton, C. Impact of risk factors on early cancer evolution. Cell 186, 1541–1563 (2023).

14. Del Poggetto, E. et al. Epithelial memory of inflammation limits tissue damage while

promoting pancreatic tumorigenesis. Science 373, eabj0486 (2021).

15. Alonso-Curbelo, D. et al. A gene-environment-induced epigenetic program initiates tumorigenesis. Nature 590, 642–648 (2021).

16. Nalio Ramos, R. et al. Tissue-resident FOLR2+

 macrophages associate with CD8+

 T cell

infiltration in human breast cancer. Cell 185, 1189–1207.e1125 (2022).

17. Montaldo, E. et al. Cellular and transcriptional dynamics of human neutrophils at steady state and upon stress. Nat. Immunol. 23, 1470–1483 (2022).

18. Hingorani, S. R. et al. Trp53R172H and KrasG12D cooperate to promote chromosomal instability

and widely metastatic pancreatic ductal adenocarcinoma in mice. Cancer Cell 7, 469–483 (2005).

19. Schiebinger, G. et al. Optimal-transport analysis of single-cell gene expression identifies developmental trajectories in reprogramming. Cell 176, 928–943.e922 (2019).

20. Lange, M. et al. CellRank for directed single-cell fate mapping. Nat. Methods 19, 159–170 (2022).

21. Liu, Z. et al. Fate mapping via Ms4a3-expression history traces monocyte-derived cells. Cell 178, 1509–1525.e1519 (2019).

22. Ostuni, R. et al. Latent enhancers activated by stimulation in differentiated cells. Cell 152, 157–171 (2013).

23. Zelenay, S. et al. Cyclooxygenase-dependent tumor growth through evasion of immunity. Cell 162, 1257–1270 (2015).

24. Perkins, D. J. et al. Autocrine-paracrine prostaglandin E2 signaling restricts TLR4 internalization and TRIF signaling. Nat. Immunol. 19, 1309–1318 (2018).

25. Cilenti, F. et al. A PGE2–MEF2A axis enables context-dependent control of inflammatory gene expression. Immunity 54, 1665–1682 (2021).

26. Zaslona, Z. et al. The induction of pro-IL-1β by lipopolysaccharide requires endogenous prostaglandin E2 production. J. Immunol. 198, 3558–3564 (2017).

27. Peng, J. et al. Single-cell RNA-seq highlights intra-tumoral heterogeneity and malignant

progression in pancreatic ductal adenocarcinoma. Cell Res. 29, 725–738 (2019).

28. Burdziak, C. et al. Epigenetic plasticity cooperates with cell-cell interactions to direct pancreatic tumorigenesis. Science 380, eadd5327 (2023).

29. Carpenter, E. S. et al. Analysis of donor pancreata defines the transcriptomic signature and microenvironment of early neoplastic lesions. Cancer Discov. 13, 1324–1345 (2023).

30. Lee, B. et al. Single-cell sequencing unveils distinct immune microenvironments with CCR6–CCL20 crosstalk in human chronic pancreatitis. Gut 71, 1831–1842 (2022).

31. Street, K. et al. Slingshot: cell lineage and pseudotime inference for single-cell transcriptomics. BMC Genomics 19, 477 (2018).

32. Browaeys, R., Saelens, W. & Saeys, Y. NicheNet: modeling intercellular communication by linking ligands to target genes. Nat. Methods 17, 159–162 (2020).

33. Gong, Z. et al. Lung fibroblasts facilitate pre-metastatic niche formation by remodeling the local immune microenvironment. Immunity 55, 1483–1500.e1489 (2022).

34. Roulis, M. et al. Paracrine orchestration of intestinal tumorigenesis by a mesenchymal niche. Nature 580, 524–529 (2020).

35. Bonavita, E. et al. Antagonistic inflammatory phenotypes dictate tumor fate and response to immune checkpoint blockade. Immunity 53, 1215–1229.e8 (2020).

36. Sattiraju, A. et al. Hypoxic niches attract and sequester tumor-associated macrophages and cytotoxic T cells and reprogram them for immunosuppression. Immunity 56, 1825–1843 (2023).

37. Liu, X. H. et al. Prostaglandin E2 induces hypoxia-inducible factor-1alpha stabilization and nuclear localization in a human prostate cancer cell line. J. Biol. Chem. 277, 50081–50086 (2002).

38. Tannahill, G. M. et al. Succinate is an inflammatory signal that induces IL-1β through HIF-1α.

Nature 496, 238–242 (2013).

39. Adler, M. et al. Principles of cell circuits for tissue repair and fibrosis. iScience 23, 100841 (2020).

40. Hangai, S. et al. PGE2 induced in and released by dying cells functions as an inhibitory DAMP. Proc. Natl Acad. Sci. USA 113, 3844–3849 (2016).

41. Li, R. et al. Mapping single-cell transcriptomes in the intra-tumoral and associated territories of kidney cancer. Cancer Cell 40, 1583–1599.e1510 (2022).

42. Chittezhath, M. et al. Molecular profiling reveals a tumor-promoting phenotype of monocytes and macrophages in human cancer progression. Immunity 41, 815–829 (2014).

43. Das, S., Shapiro, B., Vucic, E. A., Vogt, S. & Bar-Sagi, D. Tumor cell-derived IL1β promotes desmoplasia and immune suppression in pancreatic cancer. Cancer Res. 80, 1088–1101 (2020).

44. Hill, W. et al. Lung adenocarcinoma promotion by air pollutants. Nature 616, 159–167 (2023).

45. Dmitrieva-Posocco, O. et al. Cell-type-specific responses to interleukin-1 control microbial invasion and tumor-elicited inflammation in colorectal cancer. Immunity 50, 166–180.e167 (2019).

46. Garlanda, C. & Mantovani, A. Interleukin-1 in tumor progression, therapy, and prevention. Cancer Cell 39, 1023–1027 (2021).

47. Bell, C. R. et al. Chemotherapy-induced COX-2 upregulation by cancer cells defines their inflammatory properties and limits the efficacy of chemoimmunotherapy combinations. Nat. Commun. 13, 2063 (2022).

48. Nikolos, F. et al. Cell death-induced immunogenicity enhances chemoimmunotherapeutic response by converting immune-excluded into T-cell inflamed bladder tumors. Nat. Commun. 13, 1487 (2022).

49. Zhivaki, D. et al. Inflammasomes within hyperactive murine dendritic cells stimulate long-lived t cell-mediated anti-tumor immunity. Cell Rep. 33, 108381 (2020).

50. Ridker, P. M. et al. Effect of interleukin-1β inhibition with canakinumab on incident lung cancer in patients with atherosclerosis: exploratory results from a randomised, doubleblind, placebo-controlled trial. Lancet 390, 1833–1842 (2017).

51. Olive, K. P. et al. Inhibition of Hedgehog signaling enhances delivery of chemotherapy in a mouse model of pancreatic cancer. Science 324, 1457–1461 (2009).

52. Cappello, P. et al. Vaccination with ENO1 DNA prolongs survival of genetically engineered mice with pancreatic cancer. Gastroenterology 144, 1098–1106 (2013).

53. Corbett, T. H. et al. Induction and chemotherapeutic response of two transplantable ductal adenocarcinomas of the pancreas in C57BL/6 mice. Cancer Res. 44, 717–726 (1984).

54. Labun, K. et al. CHOPCHOP v3: expanding the CRISPR web toolbox beyond genome editing. Nucleic Acids Res. 47, W171–W174 (2019).

55. Pelly, V. S. et al. Anti-inflammatory drugs remodel the tumor immune environment to enhance immune checkpoint blockade efficacy. Cancer Discov. 11, 2602–2619 (2021).

56. Baker, L. A. & Tuveson, D. A. Generation and culture of tumor and metastatic organoids from murine models of pancreatic ductal adenocarcinoma. Methods Mol. Biol. 1882, 117–133 (2019).

57. Milani, M. et al. Genome editing for scalable production of alloantigen-free lentiviral vectors for in vivo gene therapy. EMBO Mol. Med. 9, 1558–1573 (2017).

58. Golovko, M. Y. & Murphy, E. J. An improved LC–MS/MS procedure for brain prostanoid analysis using brain fixation with head-focused microwave irradiation and liquid–liquid extraction. J. Lipid Res. 49, 893–902 (2008).

59. Bankhead, P. et al. QuPath: open source software for digital pathology image analysis. Sci. Rep. 7, 16878 (2017).

60. Zheng, G. X. et al. Massively parallel digital transcriptional profiling of single cells. Nat. Commun. 8, 14049 (2017).

61. Germain, P. L., Lun, A., Garcia Meixide, C., Macnair, W. & Robinson, M. D. Doublet identification in single-cell sequencing data using scDblFinder. F1000Res 10, 979 (2021).

62. Haghverdi, L., Lun, A. T. L., Morgan, M. D. & Marioni, J. C. Batch effects in single-cell RNAsequencing data are corrected by matching mutual nearest neighbors. Nat. Biotechnol. 36, 421–427 (2018).

63. Korsunsky, I. et al. Fast, sensitive and accurate integration of single-cell data with Harmony.
Nat. Methods 16, 1289–1296 (2019).

64. Becht, E. et al. Dimensionality reduction for visualizing single-cell data using UMAP. Nat. Biotechnol. 37, 38–44 (2019).

65. Gao, R. et al. Delineating copy number and clonal substructure in human tumors from

single-cell transcriptomes. Nat. Biotechnol. 39, 599–608 (2021).

66. Yu, G., Wang, L. G., Han, Y. & He, Q. Y. clusterProfiler: an R package for comparing biological

themes among gene clusters. OMICS 16, 284–287 (2012).

67. Durinck, S., Spellman, P. T., Birney, E. & Huber, W. Mapping identifiers for the integration

of genomic datasets with the R/Bioconductor package biomaRt. Nat. Protoc. 4, 1184–1191

(2009).

68. Setty, M. et al. Characterization of cell fate probabilities in single-cell data with Palantir.

Nat. Biotechnol. 37, 451–460 (2019).

69. Wolf, F. A., Angerer, P. & Theis, F. J. SCANPY: large-scale single-cell gene expression data

analysis. Genome Biol. 19, 15 (2018).

70. La Manno, G. et al. RNA velocity of single cells. Nature 560, 494–498 (2018).

71. Bergen, V., Lange, M., Peidli, S., Wolf, F. A. & Theis, F. J. Generalizing RNA velocity to transient

cell states through dynamical modeling. Nat. Biotechnol. 38, 1408–1414 (2020).

72. Reuter, B., Weber, M., Fackeldey, K., Roblitz, S. & Garcia, M. E. Generalized Markov state

modeling method for nonequilibrium biomolecular dynamics: exemplified on amyloid

beta conformational dynamics driven by an oscillating electric field. J. Chem. Theory

Comput. 14, 3579–3594 (2018).

73. Liberzon, A. et al. The Molecular Signatures Database (MSigDB) hallmark gene set collection.

Cell Syst 1, 417–425 (2015).

74. Stuart, T. et al. Comprehensive integration of single-cell data. Cell 177, 1888–1902.e1821

(2019).

75. Lopez, R. et al. DestVI identifies continuums of cell types in spatial transcriptomics data.

Nat. Biotechnol. 40, 1360–1369 (2022).

76. Dries, R. et al. Giotto: a toolbox for integrative analysis and visualization of spatial expression

data. Genome Biol. 22, 78 (2021).

77. Stirling, D. R. et al. CellProfiler 4: improvements in speed, utility and usability. BMC

Bioinformatics 22, 433 (2021).

78. Palla, G. et al. Squidpy: a scalable framework for spatial omics analysis. Nat. Methods 19, 171–178 (2022).

79. Guilliams, M. et al. Spatial proteogenomics reveals distinct and evolutionarily conserved hepatic macrophage niches. Cell 185, 379–396.e338 (2022).

80. Stringer, C., Wang, T., Michaelos, M. & Pachitariu, M. Cellpose: a generalist algorithm for cellular segmentation. Nat. Methods 18, 100–106 (2021).

81. Petukhov, V. et al. Cell segmentation in imaging-based spatial transcriptomics. Nat. Biotechnol. 40, 345–354 (2022).

82. Hahsler, M., Piekenbrock, M. & Doran, D. dbscan: fast density-based clustering with R. J Stat

Softw 91, 1–30 (2019).

83. Bergenstrahle, J., Larsson, L. & Lundeberg, J. Seamless integration of image and molecular analysis for spatial transcriptomics workflows. BMC Genomics 21, 482 (2020).

84. Carpenter, E. S. et al. Analysis of donor pancreata defines the transcriptomic signature and microenvironment of early pre-neoplastic pancreatic lesions. Cancer Discov. 13, 1324–1345 (2023).

85. Ritchie, M. E. et al. limma powers differential expression analyses for RNA-sequencing and microarray studies. Nucleic Acids Res. 43, e47 (2015).

86. Picelli, S. et al. Full-length RNA-seq from single cells using Smart-seq2. Nat. Protoc. 9, 171–181 (2014).

87. Dobin, A. et al. STAR: ultrafast universal RNA-seq aligner. Bioinformatics 29, 15–21 (2013).

88. Liao, Y., Smyth, G. K. & Shi, W. The R package Rsubread is easier, faster, cheaper and better for alignment and quantification of RNA sequencing reads. Nucleic Acids Res. 47, e47 (2019).

89. Pruitt, K. D., Tatusova, T. & Maglott, D. R. NCBI reference sequences (RefSeq): a curated non-redundant sequence database of genomes, transcripts and proteins. Nucleic Acids Res. 35, D61–65 (2007).

90. Robinson, M. D., McCarthy, D. J. & Smyth, G. K. edgeR: a Bioconductor package for

differential expression analysis of digital gene expression data. Bioinformatics 26, 139–140 (2010).

91. Robinson, M. D. & Oshlack, A. A scaling normalization method for differential expression analysis of RNA-seq data. Genome Biol. 11, R25 (2010).

92. Colaprico, A. et al. TCGAbiolinks: an R/Bioconductor package for integrative analysis of TCGA data. Nucleic Acids Res. 44, e71 (2016).

93. Newman, A. M. et al. Determining cell type abundance and expression from bulk tissues with digital cytometry. Nat. Biotechnol. 37, 773–782 (2019).
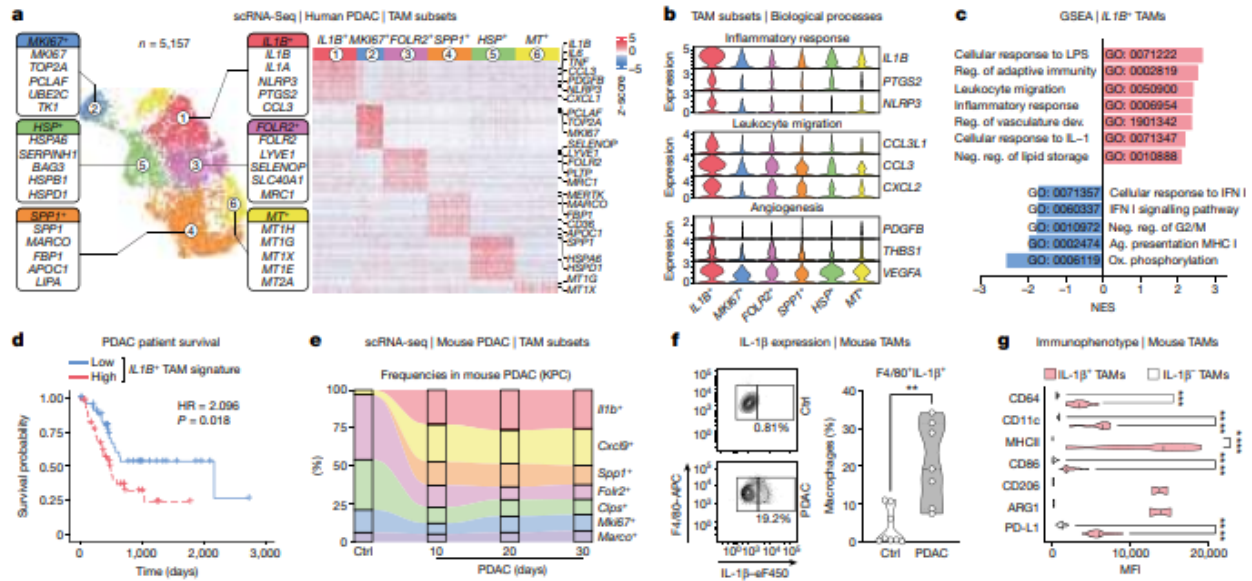
Fig. 1 | *IL1B*⁺ TAMs correlate with poor prognosis in human PDAC and are conserved in mouse models. a, Uniform manifold approximation and projection (UMAP) of scRNA-seq data from TAMs from patients with PDAC (*n* = 10) (left) and heat map of scaled expression of the top 25 marker genes for each TAM cluster (right). Colours and numbers indicate scRNA-seq clusters. **b**, Expression (scRNA-seq) of selected genes belonging to the indicated categories in TAM subsets. **c**, Gene set enrichment analysis (GSEA) (GO biological processes) on genes ranked by log₂ fold change between *IL1B*⁺ TAMs and other TAM clusters. NES, normalized enrichment score. Ag., antigen; Dev., development; neg., negative; ox., oxidative; reg., regulation. **d**, Survival probability of patients with PDAC (from TCGA data) stratified by expression

levels of the *IL1B*⁺ TAM gene signature, normalized by *CD68*. Hazard ratio (HR) and *P* value of Cox regression fit are shown. **e**, Frequencies from scRNA-seq data of TAM subsets from control pancreas (Ctrl) and PDAC (orthotopic KPC) at the indicated time points. **f**, Contour plots (left) and frequency (right) of IL-1β⁺ macrophages from control pancreas (*n* = 8) or PDAC (orthotopic KPC) (*n* = 7). Two-tailed Student's *t*-test. **g**, Expression (flow cytometry staining) of CD64, CD11c and MHCII (*n* = 8), CD206 and ARG1 (*n* = 2) and CD86 and PD-L1 (*n* = 27) within IL-1β⁺ (red) and IL-1β⁻ (white) TAMs (in subcutaneous KPC). Two-way ANOVA. MFI, median fluorescence intensity. **P* < 0.05, ***P* < 0.01, ****P* < 0.001 and *****P* < 0.0001.
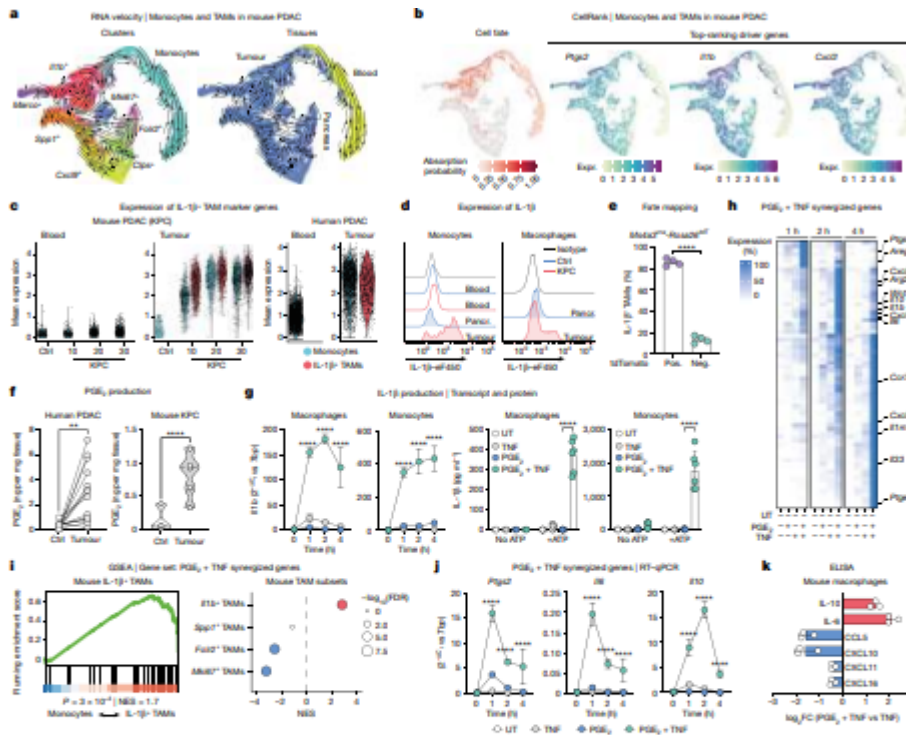
Fig. 2 | PGE₂ and TNF cooperatively elicit the IL-1β⁺ TAM state. a, RNA velocity vectors of macrophages and monocytes from blood, pancreas and PDAC (orthotopic KPC) on *t*-distributed stochastic neighbour embedding. Colours indicate cluster (left) or tissue (right) identity. **b**, Absorption probability towards *Il1b⁺* TAMs (left) and expression (expr.) of top-ranking driver genes of the monocyte-to-*Il1b⁺* TAM trajectory (right). **c**, Expression (scRNA-seq) of IL-1β⁺ TAM marker genes in monocytes and IL-1β⁺ TAMs from control pancreas and PDAC (orthotopic KPC) at the indicated time points (left) or in human monocytes and IL-1β⁺ TAMs from blood and tumour samples of patients with PDAC (right). **d**, Expression (intracellular staining) of IL-1β in monocytes and macrophages from blood, pancreas (pancr.) and PDAC (orthotopic KPC, end stage) of control (blue) or tumour-bearing (red) mice. **e**, Frequencies (mean ± s.e.m.) of tdTomato⁺ and tdTomato⁻ IL-1β⁺ TAMs from PDAC (orthotopic KPC, end stage, *n* = 4). Unpaired Student's two-tailed *t*-test. Pos., positive. **f**, Quantification of PGE₂ in human PDAC (*n* = 14) and normal

adjacent tissue (Ctrl) (*n* = 14) by enzyme-linked immunoassay (ELISA) (left; paired Student's two-tailed *t*-test) or mouse control pancreas (*n* = 3) and PDAC (orthotopic KPC, end stage) (*n* = 5) (mass spectrometry) (right; unpaired Student's two-tailed *t*-test). **g**, Transcript (left; *n* = 3) or protein (ELISA) (right; *n* = 6) expression (mean ± s.d.) of IL-1β in BMDMs or bone marrow monocytes. Two-way ANOVA. UT, untreated. **h**, Relative expression of genes synergized by PGE₂ plus TNF (Methods) in BMDMs. **i**, GSEA of genes synergized by PGE₂ plus TNF, on genes ranked by correlation with absorption probability of the monocyte-to-*Il1b⁺* TAM trajectory (left) or genes ranked by log₂ fold change between TAM subsets versus other TAMs (right). FDR, false discovery rate. **j**, Expression of the indicated genes (mean ± s.d.) in BMDMs (*n* = 3). Two-way ANOVA. **k**, Quantification (ELISA; mean ± s.d.) of the indicated proteins in the supernatant of BMDMs (*n* = 3), shown as log₂ fold change (FC) of concentration values following treatment with PGE₂ plus TNF versus TNF only.
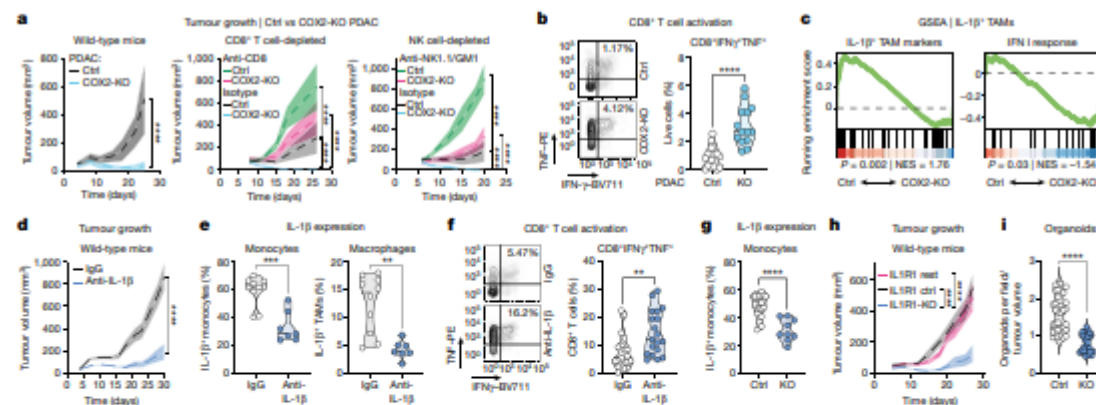

Fig. 3 | The PGE₂–IL-1β axis elicits IL-1β⁺ TAMs and promotes PDAC growth. a, Growth curves (mean ± s.d.) of control and COX2-KO PDAC cells (subcutaneous KPC) in wild-type (*n* = 5 per group), CD8⁺ T cell-depleted (*n* = 5 per group) or NK cell-depleted (*n* = 9 per group) mice. Two-way ANOVA. **b**, Contour plots (left) and frequency (right) of activated CD8⁺ T cells in tumour-draining lymph nodes of mice inoculated with control (*n* = 15) or COX2-KO (*n* = 14) PDAC (subcutaneous KPC). Unpaired *t*-test. **c**, GSEA of IL-1β⁺ TAM marker genes and type I interferon (IFN I) response genes on genes ranked by log₂ fold change between IL-1β⁺ TAMs from control versus COX2-KO PDAC (subcutaneous KPC, day 7). **d**, Growth curves (mean ± s.e.m.) of PDAC cells (subcutaneous KPC) in mice treated with anti-IL-1β or isotype control (IgG) (*n* = 10 per group). Two-way ANOVA. **e**, Frequency of tumour-infiltrating (subcutaneous KPC) IL-1β⁺ monocytes or macrophages in mice treated with

anti-IL-1β (*n* = 7) or IgG (*n* = 10). Unpaired Student's two-tailed *t*-test. **f**, Contour plots (left) and frequency (right) of activated CD8⁺ T cells in tumour-draining lymph nodes (subcutaneous KPC, end stage) of mice treated with anti-IL-1β or IgG (*n* = 19 per group). Unpaired Student's two-tailed *t*-test. **g**, Frequency of tumour-infiltrating IL-1β⁺ monocytes in mice inoculated with control (*n* = 18) or IL1R1-KO (*n* = 9) PDAC (subcutaneous KPC, end stage). Unpaired Student's two-tailed *t*-test. **h**, Growth curves (mean ± s.e.m.) of control, IL1R1-KO and IL1R1-reconstituted IL1R1-KO (IL1R1 rest) PDAC (subcutaneous KPC) in wild-type mice (*n* = 10 per group). Two-way ANOVA. **i**, Organoid-forming efficiency (organoids per field divided by tumour volume) of explanted control and IL1R1-KO PDAC (subcutaneous KPC, day 11). Tumours (*n* = 4 per group) were plated in 8 wells, 4 fields per well were counted. Unpaired Student's two-tailed *t*-test with Welch's correction.
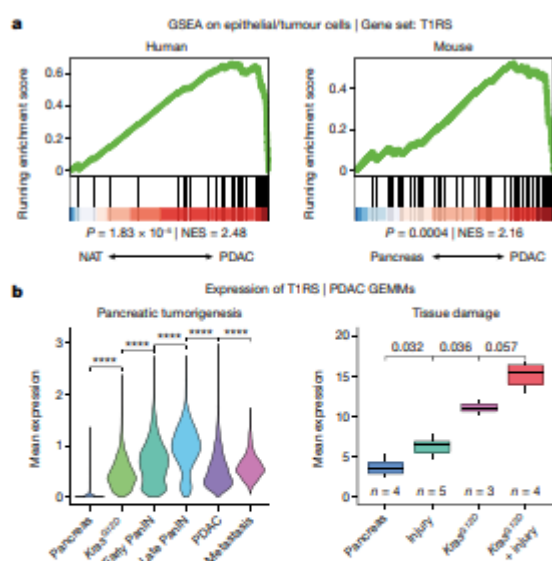
Fig. 4 | Inflammatory reprogramming occurs early during pancreatic tumorigenesis. a, GSEA of T1RS genes on genes ranked by $\log_2$FC between human PDAC and normal adjacent tissue (NAT) or between mouse PDAC and control pancreas. NES, normalized enrichment score. **b**, Expression of T1RS genes in pancreatic cells from the indicated mouse models of tumorigenesis (left) or tissue damage and oncogene activation (right). Boxes extend from the bottom quartile to top quartile values, with a line at the median. Whiskers extend from the box to show the range of the data no further than 1.5 times the inter-quartile range from the hinges. Two-sided Mann–Whitney test. Sample size (right) is indicated.
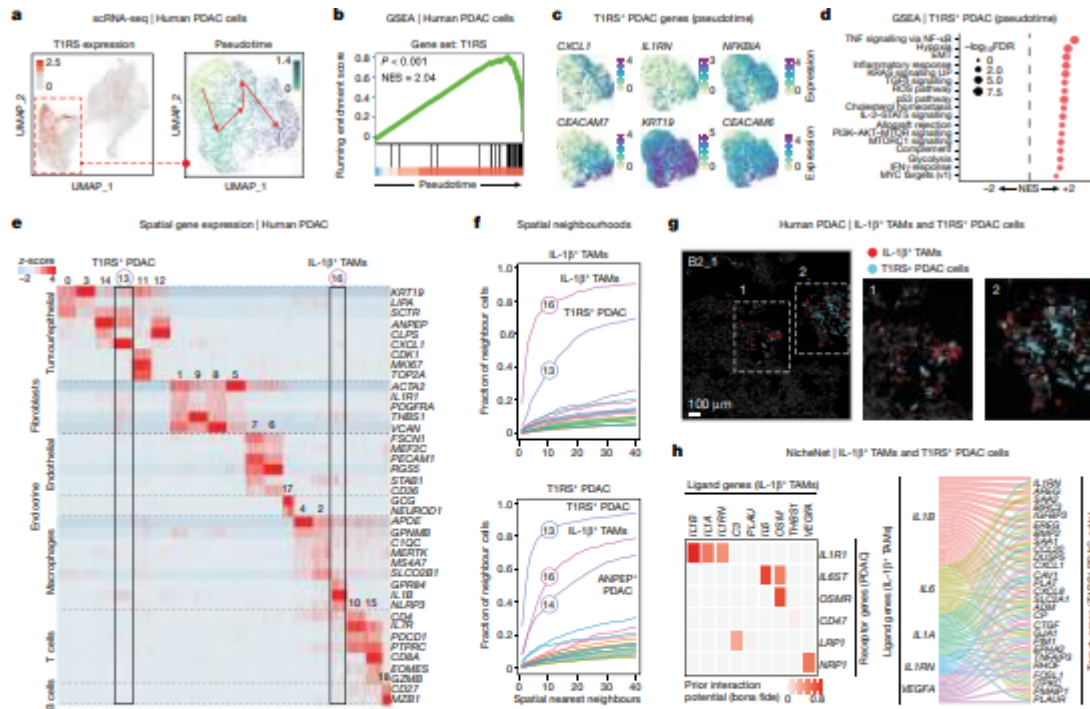
Fig. 5 | IL-1β⁺ TAMs spatially colocalize with T1RS⁺ PDAC cells in patients with PDAC. a, UMAP of scRNA-seq data of PDAC cells from chemotherapy-naive patients showing mean expression of T1RS genes (left) and pseudotime analyses (right). **b**, GSEA of T1RS genes on pseudotime-ordered genes of the computed developmental trajectory of T1RS⁺ PDAC cells. **c**, Expression of selected pseudotime-correlated T1RS genes and/or IL-1β targets in PDAC cells. **d**, GSEA of MSigDB hallmark genes on pseudotime-ordered genes of the computed developmental trajectory of T1RS⁺ PDAC cells. ROS, reactive oxygen species. **e**, Heat map of scaled expression (in situ RNA hybridization) of marker genes for clusters identified by spatial transcript analyses (Methods). Numbers refer to cluster identity. T1RS⁺ PDAC cells (cluster 13) and IL-1β⁺ TAMs (cluster 16)

are highlighted. **f**, Fraction of cells belonging to each cluster identified by spatial transcript analyses (Methods) found in the spatial neighbourhood of IL-1β⁺ TAMs (top) or T1RS⁺ PDAC cells (bottom). Numbers and colours refer to cluster identity. **g**, Selected regions of interest (ROIs) (LPDAC30 B2_1) showing co-localization of IL-1β⁺ TAMs and T1RS⁺ PDAC cells in spatial gene expression analyses. The numbered regions of interest (left) are magnified (right). **h**, Left, heat map of interaction potential (NicheNet) between top-ranking ligands (Methods) expressed by IL-1β⁺ TAMs and cognate receptors on PDAC cells. Right, alluvial plot showing the top five ligands expressed by IL-1β⁺ TAMs ranked by overall regulatory potential, and their connection with predicted target genes expressed by T1RS⁺ PDAC cells.
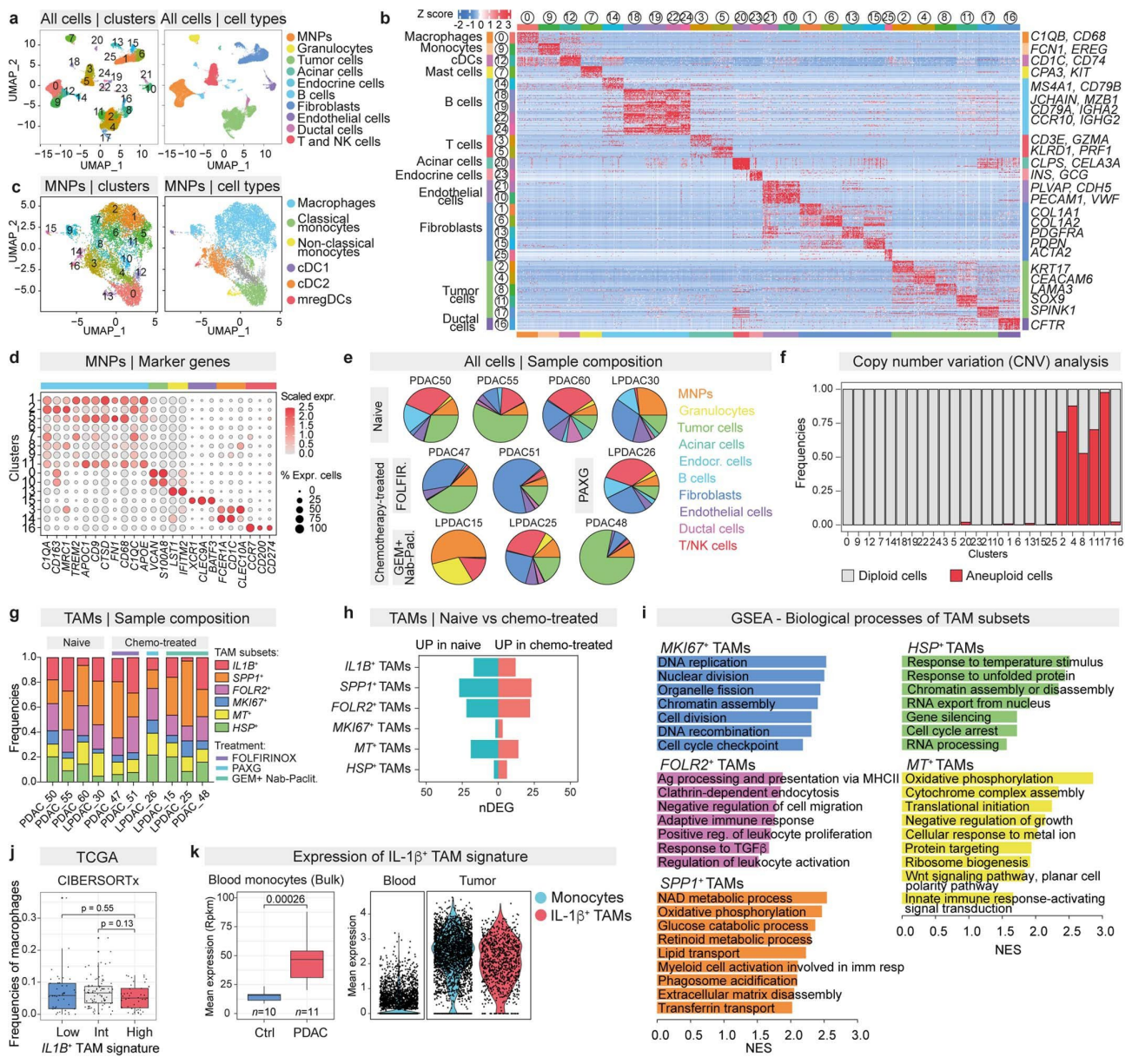
Extended Data Fig. 1: scRNA-seq analyses of PDAC patients.

a, UMAP of scRNA-Seq of all cells from PDAC patients. Colors and numbers indicate scRNA-Seq clusters (left) or cell type annotations (right). b, Heatmap of scaled expression of top 25 marker genes for each scRNA-Seq cluster. Selected transcripts are indicated. c, UMAP of scRNA-Seq of mononuclear phagocytes (MNPs) from PDAC patients. Colors and numbers indicate scRNA-Seq clusters (left) or cell type annotations (right). d, Dot plot of scaled expression of selected marker genes for each MNP cluster. e, Relative abundance (scRNA-Seq) of the indicated cell types for individual naïve or chemotherapy-treated PDAC patients. GEM+Nab-Pacl., gemcitabine+Nab-paclitaxel; FOLFIR., FOLFIRINOX; PAXG, cisplatin+Nab-paclitaxel, capecitabine, gemcitabine. f, Frequencies of diploid or aneuploid cells for each cluster, as predicted by copy number variation (CNV) analysis with CopyKAT. g, Frequencies of TAM subsets (scRNA-Seq) for individual naïve or chemotherapy-treated PDAC patients. GEM+Nab-Pacl., gemcitabine+Nab-paclitaxel; FOLFIR., FOLFIRINOX; PAXG, cisplatin+Nab-paclitaxel, capecitabine, gemcitabine. h, Number of differentially expressed genes (DEGs) in

TAM subsets between chemotherapy-treated and naïve PDAC patients. i) GSEA (Gene Ontologies biological processes, GO BP) on genes ranked by log2FC between each TAM subset versus other TAMs. NES, Normalized Enrichment Score. j, Calculated frequencies of macrophages (CIBERSORTx deconvolution) in TCGA PDAC patients stratified according to expression levels of the IL1B+ TAM gene signature. Significance is computed by two-sided Mann-Whitney test. The box extends from the lower to upper quartile values of the data, with a line at the median. The whiskers extend from the box to show the range of the data no further than 1.5 * IQR (Inter-quartile range) from the hinges. k, Mean expression of the IL1B+ TAM gene signature in blood monocytes (bulk RNA-Seq) from healthy donors (Ctrl, n = 10) and PDAC patients (left, n = 11), and in blood or tumor monocytes or IL-1β+ TAMs from PDAC patients (right). Significance is computed by two-sided Mann-Whitney test. Sample size is indicated. The box extends from the lower to upper quartile values of the data, with a line at the median. The whiskers extend from the box to show the range of the data no further than 1.5 * IQR (Inter-quartile range) from the hinges.
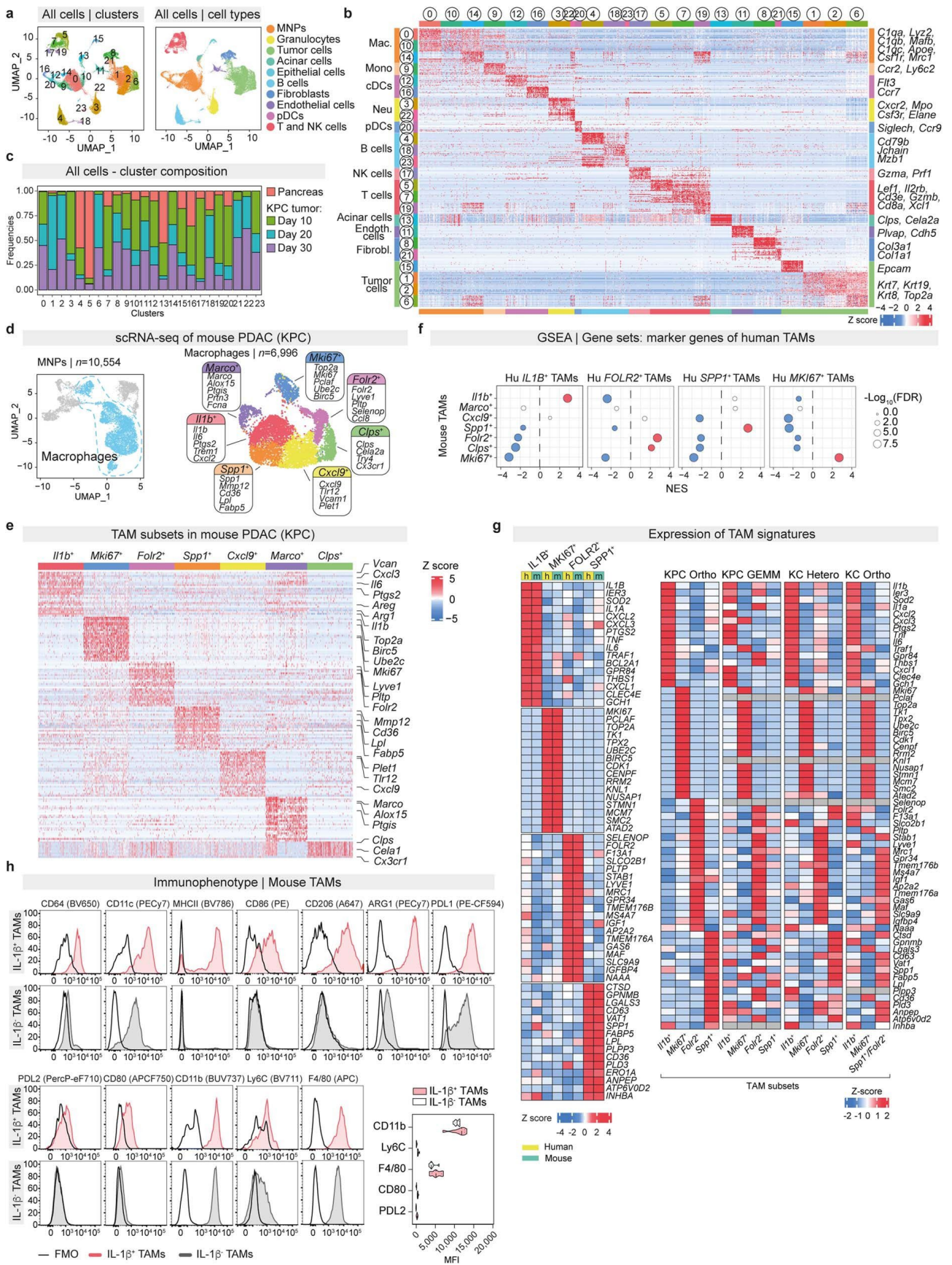
Extended Data Fig. 2: scRNA-seq analyses of mouse PDAC models.

a, UMAP of scRNA-Seq of all cells from mouse PDAC (orthotopic KPC). Colors and numbers indicate scRNA-Seq clusters (left) or cell type annotations (right). b, Heatmap of scaled

expression of top 25 marker genes for each scRNA-Seq cluster. Selected transcripts are indicated. c, Frequencies (scRNA-Seq) of cells from the indicated experimental conditions and time points in each cluster. d, UMAP of scRNA-Seq of mononuclear phagocytes (MNPs) (left) or macrophages (right) from mouse PDAC (orthotopic KPC). e, Heatmap of scaled expression of top 25 marker genes for each mouse TAM subset. Selected transcripts are indicated. f, GSEA (marker genes of human TAM subsets) on genes ranked by log2FC between each mouse TAM subset versus other TAMs. NES, Normalized Enrichment Score. g, Heatmap of scaled gene expression of species-conserved marker genes in human or mouse TAM subsets (left), or in mouse TAM subsets from the indicated PDAC models (right). Only clusters of TAMs conserved between species are reported. h, Expression (flow cytometry) of the indicated markers (CD11b, Ly6C and F4/80, n = 8; CD80 and PD-L2, n = 27) by IL-1β+ TAMs (red) and IL-1β- TAMs (grey). Representative histograms and median fluorescence intensity (MFI) values are shown. Black lines represent fluorescence minus one control (FMO).
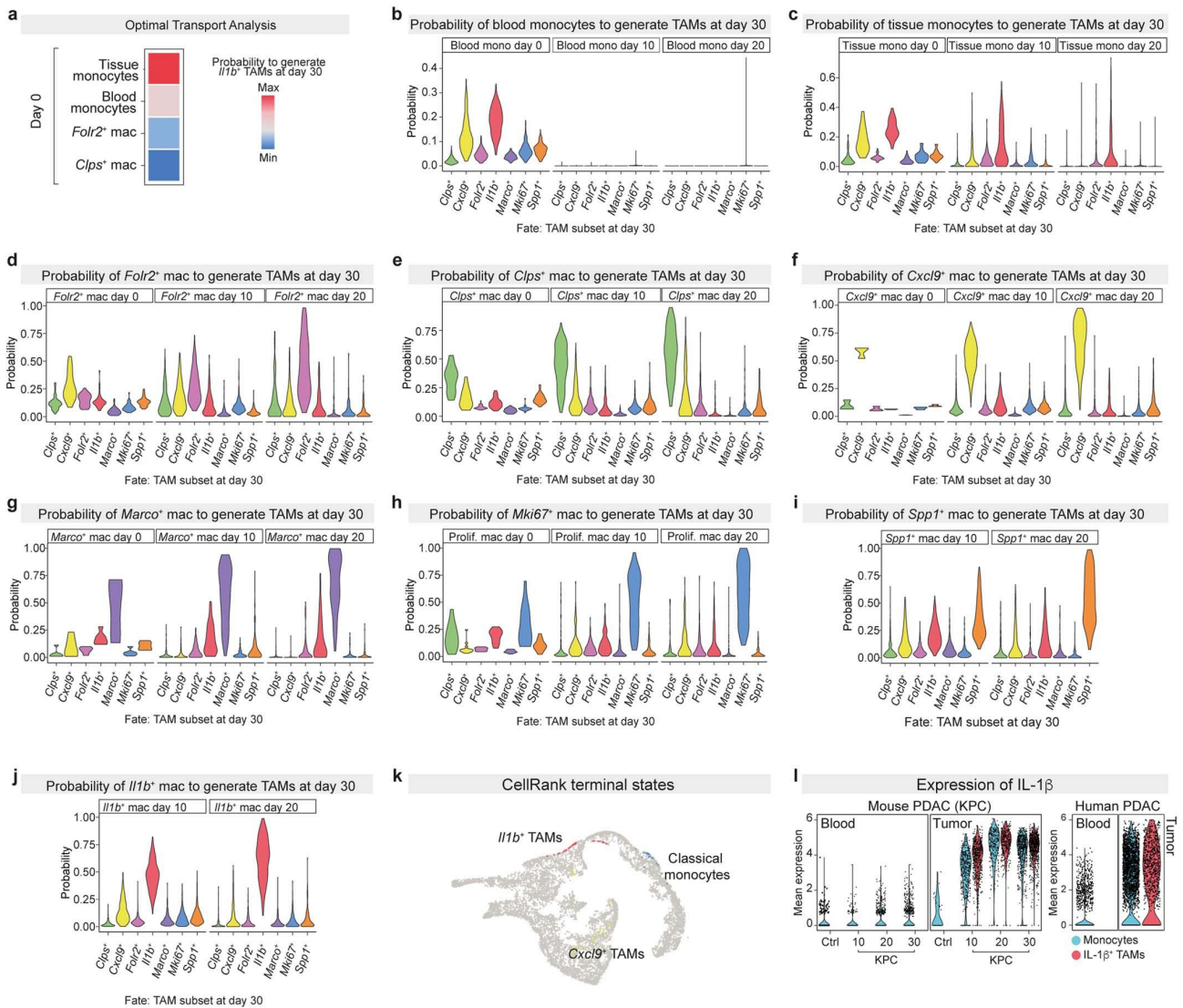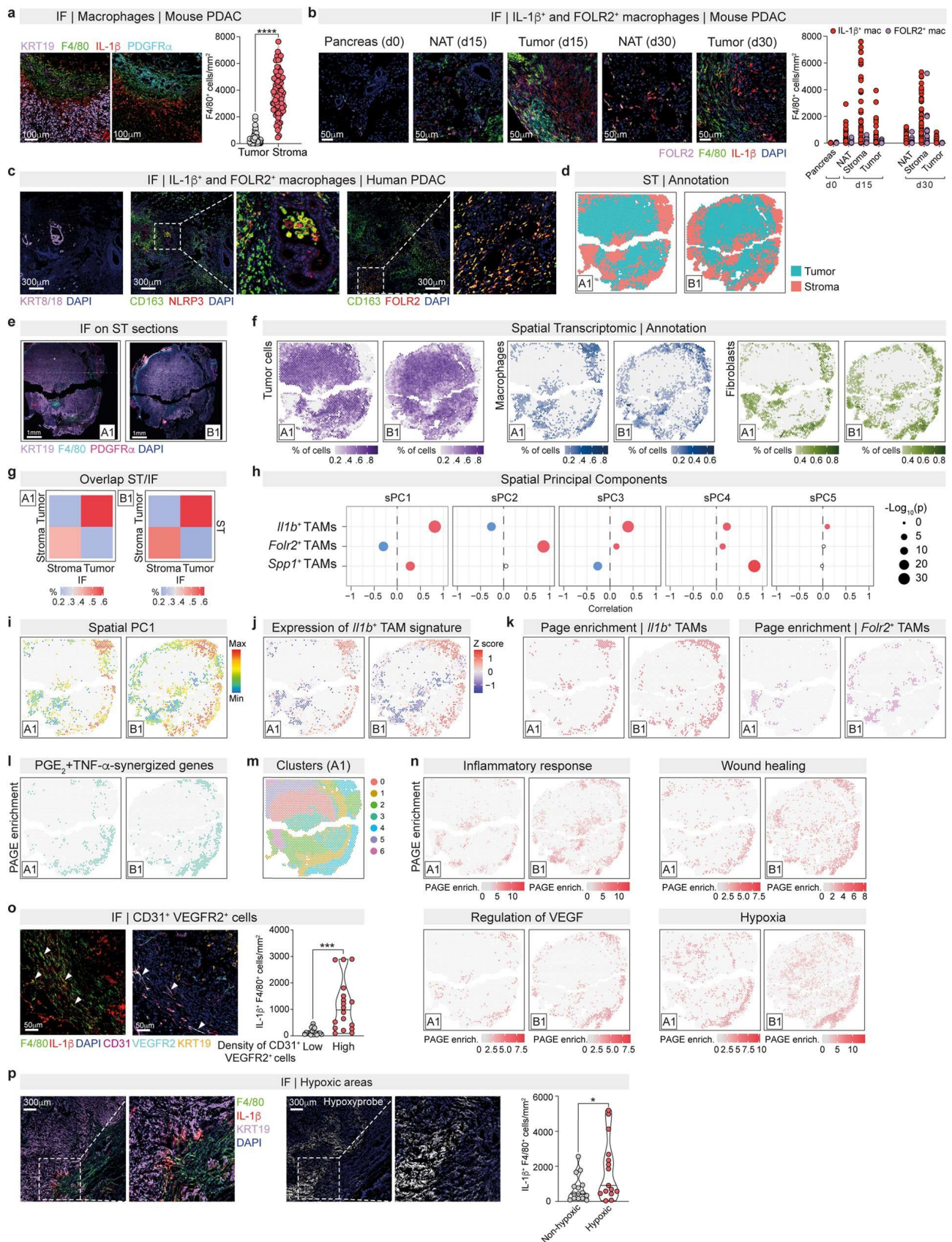
Extended Data Fig. 3: Ontogeny of IL-1β+ TAMs.

a, Scaled mean fate probabilities (Optimal Transport Analysis, OTA) to acquire IL-1β+ TAM identity (at day 30) for the indicated cell populations in mouse PDAC (orthotopic KPC). **b-j**, Fate probabilities (OTA) to acquire the transcriptional programs of the indicated TAM subsets in mouse PDAC (orthotopic KPC) by blood monocytes (**b**), tissue monocytes (**c**), *Folr2*+ macrophages (**d**), *Clps*+ macrophages (**e**), *Cxcl9*+ macrophages (**f**), *Marco*+ macrophages (**g**), *Mki67*+ macrophages (**h**), *Spp1*+ TAMs (**i**) and *Il1b*+ TAMs (**j**). Probability values are shown for all time points. **k**, Cells identified as terminal states (CellRank) in tSNE embedding of mouse macrophages and monocytes from tissue and blood samples. **i,** Mean expression (scRNA-Seq) of *Il1b* in monocytes and IL-1β+ TAMs from control pancreas (Ctrl) and PDAC (orthotopic KPC) at the indicated time points (left), or in human monocytes and IL-1β+ TAMs from blood and tumor samples of PDAC patients (right).
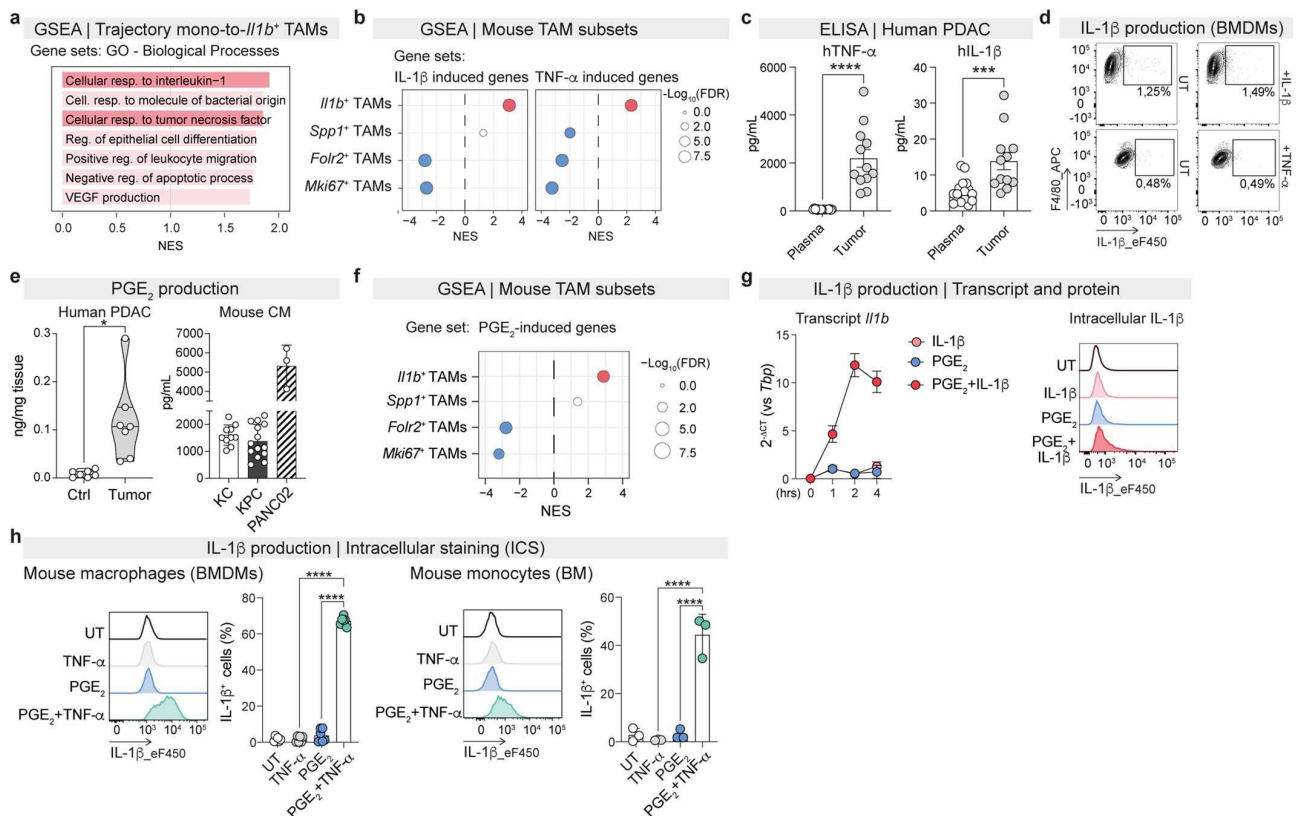
Extended Data Fig. 4: Elicitation of the IL-1β+ TAM state by PGE2 and TNF-α.

a, GSEA (GO BP) on genes ranked by correlation with absorption probability of the monocyte-to-Il1b+ TAM transition. Selected terms are shown. b, GSEA on genes ranked by log2FC between each mouse TAM subset versus other TAMs. Gene sets: IL-1β-induced or TNF-α-induced genes. NES, Normalized Enrichment Score. c, Concentration (mean ± SEM) of TNF-α (n = 18) and IL-1β (n = 17) in plasma and tumor of PDAC patients (n = 12). ***p < 0.001 ****p < 0.0001 (unpaired student's two-tailed t test). d, Expression of IL-1β (intracellular staining) in mouse BMDMs treated for 6 h with IL-1β or TNF-α. e, Quantification of PGE2 in human PDAC samples and control (Ctrl) matched normal adjacent tissue (n = 7/group) by mass spectrometry (left), or in culture supernatants of KPC (n = 14), KC (n = 10) and PANC02 (n = 3) PDAC cells by ELISA (mean±SD, right). *p < 0.05 (paired student's two-tailed t test). f, GSEA (PGE2-induced genes) on genes ranked by log2FC between each mouse TAM subset versus other TAMs (orthotopic KPC). NES, Normalized Enrichment Score. g, Transcript (mean ± SD, left) or protein (intracellular staining, right) expression of IL-1β in BMDMs stimulated as indicated (n = 2). h, Expression (intracellular staining) of IL-1β in BMDMs (n = 6, left) or BM monocytes (n = 3, right) stimulated as indicated. ****p < 0.0001 (one-way ANOVA).

Extended Data Fig. 5: Spatial distribution of IL-1β+ TAMs.

a, Left panels. Selected regions of interest showing signal intensity (IF staining) of KRT19 (tumor cells), F4/80 (macrophages), PDGFR-α (fibroblasts) and IL-1β in mouse PDAC (orthotopic KPC, end-stage). Right panels. Quantification of macrophages (cells/mm2) in

stromal or tumor areas (n = 2 mice, n = 4 sections/mouse, n = 10 ROI/area). ****p < 0.0001 (unpaired student's two-tailed t test). b, Left panels. Selected regions of interest showing signal intensity (IF staining) of FOLR2, F4/80, IL-1β, and DAPI in control pancreas (day 0), mouse PDAC (orthotopic KPC), or normal adjacent tissue (NAT) at the indicated time points. Right panels. Quantification of IL-1β+ and FOLR2+ macrophages (cells/mm2) in stromal, tumor areas or NAT areas. Ctrl pancreas, n = 2 mice, n = 2 sections/mouse, n = 10 ROI/section; Day 15 PDAC, n = 4 mice, n = 2 sections/mouse, n = 5 ROI/areas; Day 30 PDAC, n = 5 mice, n = 2 sections/mouse, n = 10 ROI/areas. c, Selected regions of interest with inset magnifications showing signal intensity (IF staining) of KRT8-18, CD163, NLRP3, and DAPI (middle), or CD163, FOLR2 and DAPI (right) on consecutive sections of human PDAC samples. d, Annotation (see Methods) of tumor or stromal areas in spatial transcriptomics data (Visium) for the indicated tissue sections of mouse PDAC (orthotopic KPC, end-stage). e, Signal intensity (IF staining) of KRT19, F4/80, PDGFR-α and DAPI for the indicated tissue sections of mouse PDAC (orthotopic KPC, end-stage). f, Percentages (DestVI deconvolution) of tumor cells (left), macrophages (middle) and fibroblasts (right) in spatial transcriptomics data (Visium) for the indicated tissue sections of mouse PDAC (orthotopic KPC, end-stage). g, Percentage of spots with concordant annotation as stroma or tumor by spatial transcriptomics (Visium) and IF staining for the indicated tissue sections of mouse PDAC (orthotopic KPC, end-stage). h, Correlation values (red, positive; blue, negative; white, non-significant) between mean gene expression (Visium) of marker genes of the indicated TAM subsets (DestVI generative model, see Methods) and spatial principal components (sPC) coordinates for spots of a selected tissue section (A1) of mouse PDAC (orthotopic KPC, end-stage). i, Coordinates of spatial Principal Component 1 (sPC1) of macrophage-enriched spots (DestVI deconvolution) in spatial transcriptomics data (Visium) for the indicated tissue sections of mouse PDAC (orthotopic KPC, end-stage). j, Scaled mean expression of marker genes of IL-1β+ TAMs (DestVI generative model) in macrophage-enriched spots (DestVI deconvolution) in spatial transcriptomics data (Visium) for the indicated tissue sections of mouse PDAC (orthotopic KPC, end-stage). k, Enrichment (PAGE) of expression of marker genes of IL-1β+ TAMs (left) or FOLR2+ TAMs (right) in macrophage-enriched spots (DestVI deconvolution) in spatial transcriptomics data (Visium) for the indicated tissue sections of mouse PDAC (orthotopic KPC, end-stage). Colors indicate macrophage-enriched ST spots with significance (estimated on all spots) of p < 0.001. l, Enrichment (PAGE) of expression of PGE2 + TNF-α synergized genes in macrophage-enriched spots (DestVI deconvolution) in spatial transcriptomics data (Visium) for the indicated tissue sections of mouse PDAC (orthotopic KPC, end-stage). Colors indicate macrophage-enriched ST spots with significance (estimated on all spots) of p < 0.001. m, Louvain clustering of spots in spatial transcriptomics data (Visium) for a selected tissue section (A1) of mouse PDAC (orthotopic KPC, end-stage). n, Enrichment (PAGE) of expression of genes belonging to the indicated GO BPs in spatial transcriptomics data (Visium) for the indicated tissue sections of mouse PDAC (orthotopic KPC, end-stage). GSEA was performed on genes ranked by log2FC between cluster 4 versus other spots. Colors indicate spots with significance (estimated on all spots) of p < 0.001. o, Signal intensity (IF staining) of F4/80, IL-1β, and DAPI (left), or of CD31, VEGFR2 and KRT19 (middle) in consecutive sections of mouse PDAC (orthotopic KPC, end-stage). Arrows indicate IL-1β+ F4/80+ cells (left) and CD31+ VEGFR2+ cells (middle). Quantification of IL-1β+ F4/80+ cells in areas with high and low density of CD31+ VEGFR2+ cells (right, n = 5 mice, n = 2

sections/mouse). ***p < 0.001 (unpaired student's two tailed t test). p, Signal intensity (IF staining) of F4/80, IL-1β and KRT19 (left), or of anti-Hypoxyprobe (middle) in consecutive sections of mouse PDAC (orthotopic KPC, end-stage). Quantification of IL-1β+ F4/80+ cells in hypoxic and non-hypoxic areas (right, n = 3 mice, n = 2 sections/mouse). *p < 0.05 (unpaired student's two tailed t test).
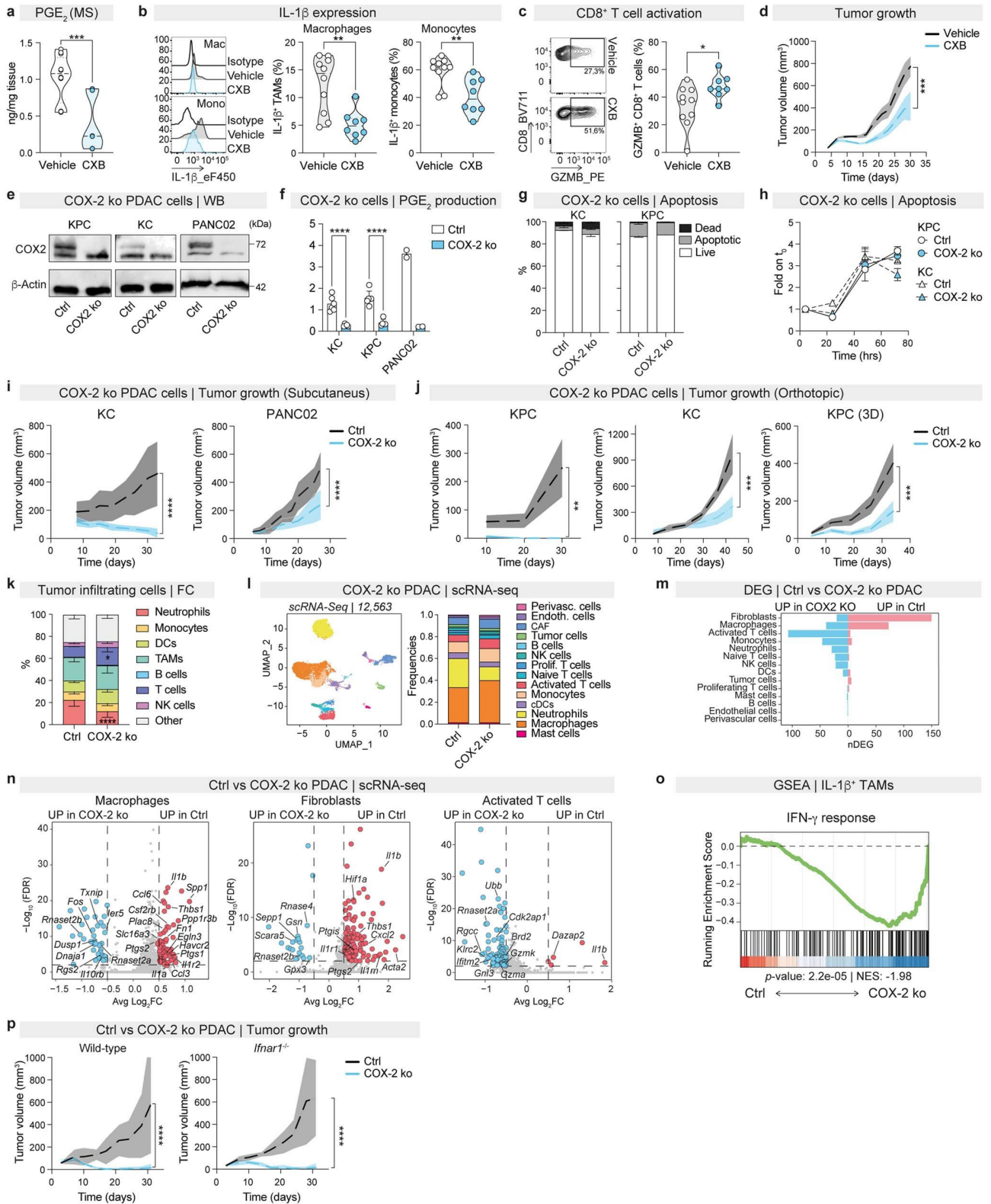
Extended Data Fig. 6: Targeting PGE2 reprograms the pancreatic TME.

a, Quantification of PGE2 (mass spectrometry) in lysates of mouse PDAC (subcutaneous KPC, end-stage) from mice treated with celecoxib (CXB, n = 3) or vehicle (n = 4). ***p < 0.001 (unpaired student's two tailed t test). b, Expression of IL-1β (intracellular staining) in macrophages and monocytes in mouse PDAC (subcutaneous KPC, end-stage) from mice treated with celecoxib (CXB, n = 8) or vehicle (n = 10). **p < 0.01 (unpaired t test). c, Contour plots (left) and frequency (right) of GZMB+ CD8+ T cells in mouse PDAC (subcutaneous KPC, end-stage) from mice treated with celecoxib (CXB, n = 8) or vehicle (n = 10). *p < 0.05 (unpaired student's two tailed t test). d, Growth curves (mean±SEM) of mouse PDAC (subcutaneous KPC) in mice treated with celecoxib (CXB, n = 10) or vehicle (n = 10). ***p < 0.001 (two-way ANOVA). e, Expression (western blot) of COX-2 and β-Actin in the indicated control and COX-2 ko mouse PDAC cell lines. f, Quantification of PGE2 (ELISA, mean±SD) in the culture supernatant of the indicated control (KC, n = 6; KPC, n = 6; PANC02, n = 2) and COX-2 KO (KC, n = 5; KPC, n = 5; PANC02, n = 2) mouse PDAC cell lines. ****p < 0.0001 (2-way ANOVA). g, Expression (mean±SD) of Annexin V and/or 7AAD cells by the indicated control (n = 2) and COX-2 ko (n = 2) mouse PDAC cells. h, Proliferation in vitro (WST-1 assay, mean±SEM) of the indicated control (n = 2) and COX-2 ko (n = 2) mouse PDAC cells. i, Growth curves (mean±SD) of control (subcutaneous KC, n = 8; subcutaneous PANC02, n = 10) and COX-2 ko PDAC cells (subcutaneous KC, n = 10; subcutaneous PANC02, n = 7) in wild-type mice. ****p < 0.0001 (two-way ANOVA). j, Growth curves (mean ± SEM) of control (Ctrl) and COX-2 ko PDAC cells (orthotopic KPC, n = 5/group, left; orthotopic KC, n = 4/group, middle) or spheroids (3D, orthotopic KPC, n = 9/group, right) in wild-type mice. **p < 0.01, ***p < 0.001 (two-way ANOVA). k, Frequencies (flow cytometry) of the indicated cell types in control or COX-2 ko PDAC (subcutaneous KPC, day 6, n = 5/group). *p < 0.05, ****p < 0.0001 (two-way ANOVA). l, UMAP showing clustering (left) and bar plots showing frequencies (right, scRNA-Seq) of the indicated cell types in control or COX-2 ko PDAC (subcutaneous KPC, day 7). m, Number of differentially expressed genes (DEG, scRNA-Seq) for the indicated cell types between control and COX-2 ko PDAC (subcutaneous KPC, day 7). n, Volcano plots of differentially expressed genes for macrophages (left), fibroblasts (middle) and activated T cells (right) between control (Ctrl) and COX-2 ko PDAC (subcutaneous KPC, day 7). Selected genes for each population are highlighted. FC, fold change. FDR, false discovery rate. o, GSEA (IFN-γ response genes,) on genes ranked by log2FC between IL-1β+ TAMs from control (Ctrl) versus COX-2 ko PDAC (subcutaneous KPC, day 7). NES, Normalized Enrichment Score. p, Growth curves (mean ± SD) of control (Ctrl) and COX-2 ko PDAC cells (subcutaneous KPC) in wild-type mice (n = 4 Ctrl, n = 5 COX-2 ko, left) or Ifnar1−/− (n = 5 Ctrl, n = 5 COX-2 ko, right) mice. ****p < 0.0001 (two-way ANOVA).
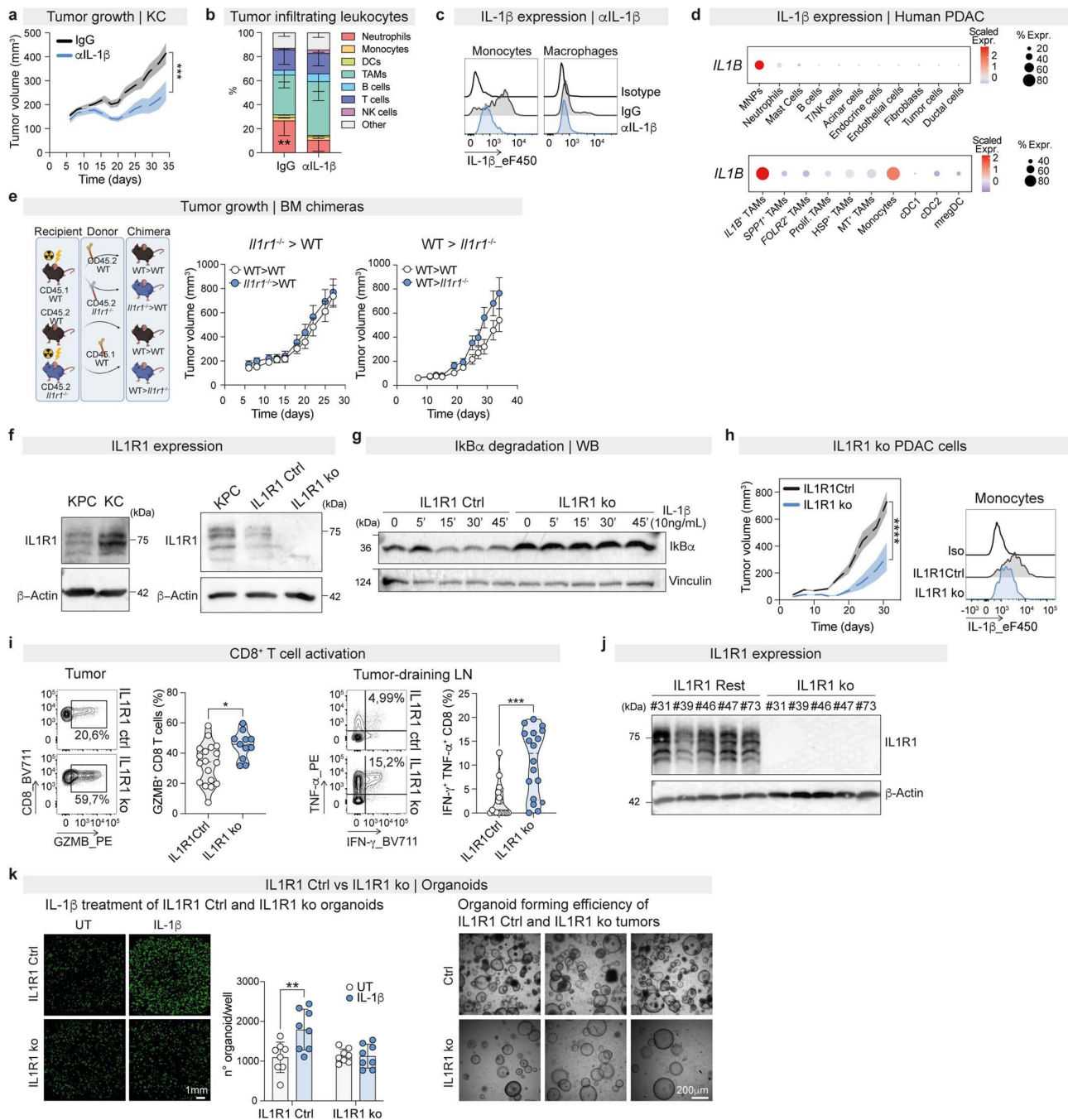
Extended Data Fig. 7: Tumor cell-intrinsic IL-1β signaling promotes PDAC growth.

a, Growth curves (mean±SEM) of PDAC cells (subcutaneous KC) in mice treated with anti-IL-1β (n = 8) or isotype control (IgG, n = 10). ***p < 0.001 (two-way ANOVA). b, Frequencies (flow cytometry, mean±SD) of the indicated cell types in PDAC (subcutaneous KPC, end-stage) of mice treated with anti-IL-1β (n = 7) or isotype control (IgG, n = 10). **p < 0.01 (two-way ANOVA). c, Expression of IL-1β (intracellular staining) in monocytes (left) or macrophages (right) in PDAC (subcutaneous KPC, end-stage) of mice treated with anti-IL-1β or isotype control (IgG). d, Dot plots of scaled IL1B expression (scRNA-Seq) in the indicated cell populations (top) or myeloid cell subsets (bottom) in human PDAC samples. e, Schematic representation (left) and growth curves (mean ± SEM) of PDAC (subcutaneous KPC) in the indicated bone marrow (BM) chimeric mice (n = 10 WT > WT, Il1r1−/−>WT; n = 11 WT> Il1r1−/) (two-way ANOVA). f, Expression of IL-1R1 and β-actin (western blot) in whole cell lysates of

the indicated parental, control (Ctrl) or IL-1R1 ko PDAC cells. g, Expression of IκBα (western blot) in whole cell lysates of control or IL-1R1 ko PDAC cells (KPC) upon stimulation with IL-1β for the indicated time points. h, Growth curves of tumors (mean ± SEM, right) and expression of IL-1β in tumor-infiltrating monocytes (intracellular staining, right) from control (Ctrl) or IL1-R1 ko PDAC (subcutaneous KPC, n = 8/group). ****p < 0.0001 (two-way ANOVA). i, Contour plots (left) and frequencies (right) of activated CD8+ T cells in tumors (subcutaneous KPC, n = 18 Ctrl, n = 11 IL-1R1 ko, left) or tumor-draining lymph nodes (subcutaneous KPC, n = 18 Ctrl, n = 18 IL-1R1 ko, right) from control (Ctrl) or IL1-R1 ko PDAC. ***p < 0.001, * p < 0.05 (unpaired student's two-tailed t test). j, Expression of IL-1R1 and β-actin (western blot) in whole cell lysates of IL-1R1 ko or IL-1R1-reconstituted IL-1R1 ko (IL1R1 Rest) PDAC (KPC) cells. Numbers denote clone ID. k, Representative images (left) and quantification (mean ± SD, middle) of organoids generated from control (Ctrl) and IL-1R1 ko PDAC cells (KPC) treated with vehicle or with IL-1β for 5 days (n = 8 wells/condition; the entire Matrigel area was collected for each well). **p < 0.01 (2-way ANOVA). Representative images (right) of organoids generated from explanted control (Ctrl) and IL-1R1 ko PDAC (subcutaneous KPC, day 11).
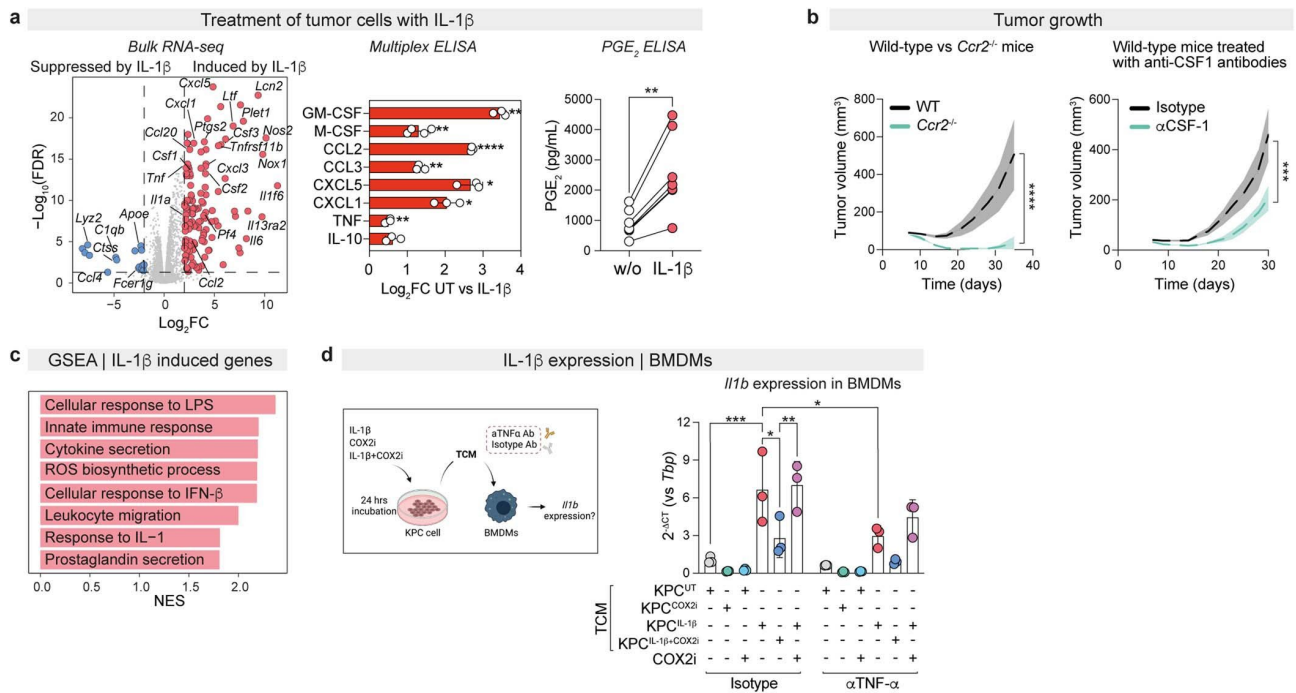
Extended Data Fig. 8: Consequences of IL-1β signaling in tumor cells.

a, Volcano plot (left) of genes up-regulated (red) or down-regulated (blue) in PDAC (KPC) cells treated with IL-1β for 24 h (UT n = 3, IL-1β n = 2). Selected genes are highlighted. Quantification (ELISA) of the indicated cytokines (mean ± SD, n = 3, unpaired two-tailed student's t test, middle) or PGE2 (n = 7, paired two-tailed student's t test, right) in the supernatant of PDAC cells (KPC) cells treated with IL-1β 24 h. *p < 0.5, **p < 0.01, ****p < 0.0001. b, Growth curves (mean±SEM) of PDAC cells (subcutaneous KPC) in wild-type and Ccr2−/− mice (left, n = 5/group) or in wild-type mice treated with an anti-CSF-1 antibody (αCSF-1, n = 8) or isotype control (IgG, n = 10). ****p < 0.0001 (two-way ANOVA). c, GSEA (GO BP) on genes ranked by log2FC between PDAC cells (KPC) treated with IL-1β versus untreated controls. NES,

Normalized Enrichment Score. d, Scheme of the experiment (left) and expression of Il1b (RT-qPCR, mean±SD) in BMDMs treated for 2 h with tumor-conditioned media (TCM) of mouse PDAC cells (KPC) from the following conditions: untreated (KPCUT) or treated for 24 h with a COX-2 inhibitor (KPCCOX2i), IL-1β (KPCIL-1β), IL-1β + COX-2 inhibitor (KPCIL-1β+COX2i). A control condition of BMDMs stimulated with vehicle or COX-2 inhibitor (COX2i) is shown. Isotype control or an anti-TNF-α antibody (αTNF-α) groups were included for each condition (n = 3). *p < 0.05 **p < 0.01 ***p < 0.001 (two-way ANOVA).
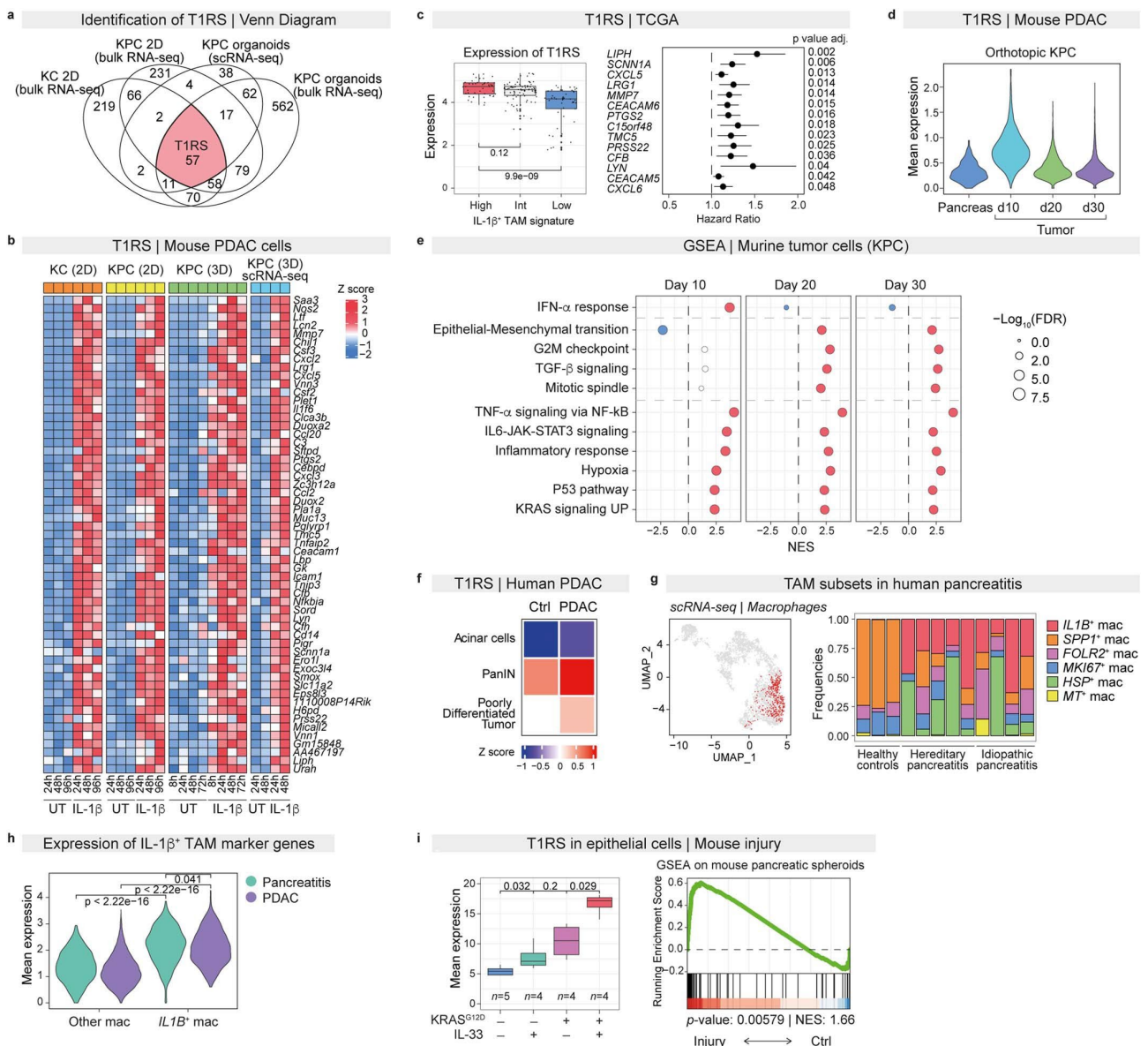
Extended Data Fig. 9: Inflammatory reprogramming of PDAC cells.

a, Venn diagram of genes up-regulated (bulk RNA-Seq or scRNA-Seq) upon treatment with IL-1β in the indicated mouse PDAC models. The tumor-intrinsic IL-1β response signature (T1RS) is composed by the 57 genes commonly up-regulated by IL-1β in all conditions. b, Heatmap of

scaled expression (bulk RNA-Seq or scRNA-Seq) of T1RS genes in the indicated mouse PDAC models, left untreated or stimulated with IL-1β for the indicated time points. c, Mean expression of human orthologs of T1RS genes (TCGA) in PDAC patients stratified for the levels of expression of the IL1B+ TAM signature (left). The box extends from the lower to upper quartile values of the data, with a line at the median. The whiskers extend from the box to show the range of the data no further than 1.5 * IQR (Inter-quartile range) from the hinges. Hazard ratios (right) obtained by fitting univariate Cox model on gene expression of T1RS genes in TCGA PDAC cohort. Only genes with significant adjusted p-values are reported. d, Mean expression (scRNA-Seq) of T1RS genes in pancreatic epithelial cells and tumor cells from control pancreas or mouse PDAC (orthotopic KPC) in the indicated time points. e, GSEA (MSigDB hallmark genes) on genes ranked by log2FC between tumor versus healthy pancreas cells at the indicated time points (orthotopic KPC). NES, Normalized Enrichment Score. FDR, False Discovery Rate. f, Heatmap of scaled mean expression (GeoMx) of human orthologs of T1RS genes in the indicated regions of interest (ROIs) of healthy donors and PDAC patients. PanIN, pancreatic intraepithelial neoplasia. g, UMAP (left) and frequencies (scRNA-Seq, right) of the indicated macrophage subsets in the pancreas of healthy controls or patient with hereditary or idiopathic pancreatitis). Cells corresponding to IL-1β+ TAMs are annotated in red. h, Mean expression (scRNA-Seq) of IL-1β+ TAM marker genes in IL-1β+ TAMs (or other TAMs) from PDAC patients and in macrophages corresponding to IL-1β+ TAMs (or other macrophages) in pancreatitis patients. Significance is computed by two-sided Mann-Whitney test. i, Left, mean expression of T1RS genes in pancreatic epithelial cells from mice control or mutated Kras and treated with vehicle or IL-33. Significance (two-sided Mann-Whitney test) is shown. Sample size is indicated. The box extends from the lower to upper quartile values of the data, with a line at the median. The whiskers extend from the box to show the range of the data no further than 1.5 * IQR (Inter-quartile range) from the hinges. Right, GSEA (T1RS genes) on genes ranked by log2FC between spheroids generated from injured or control pancreas. NES, Normalized Enrichment Score.
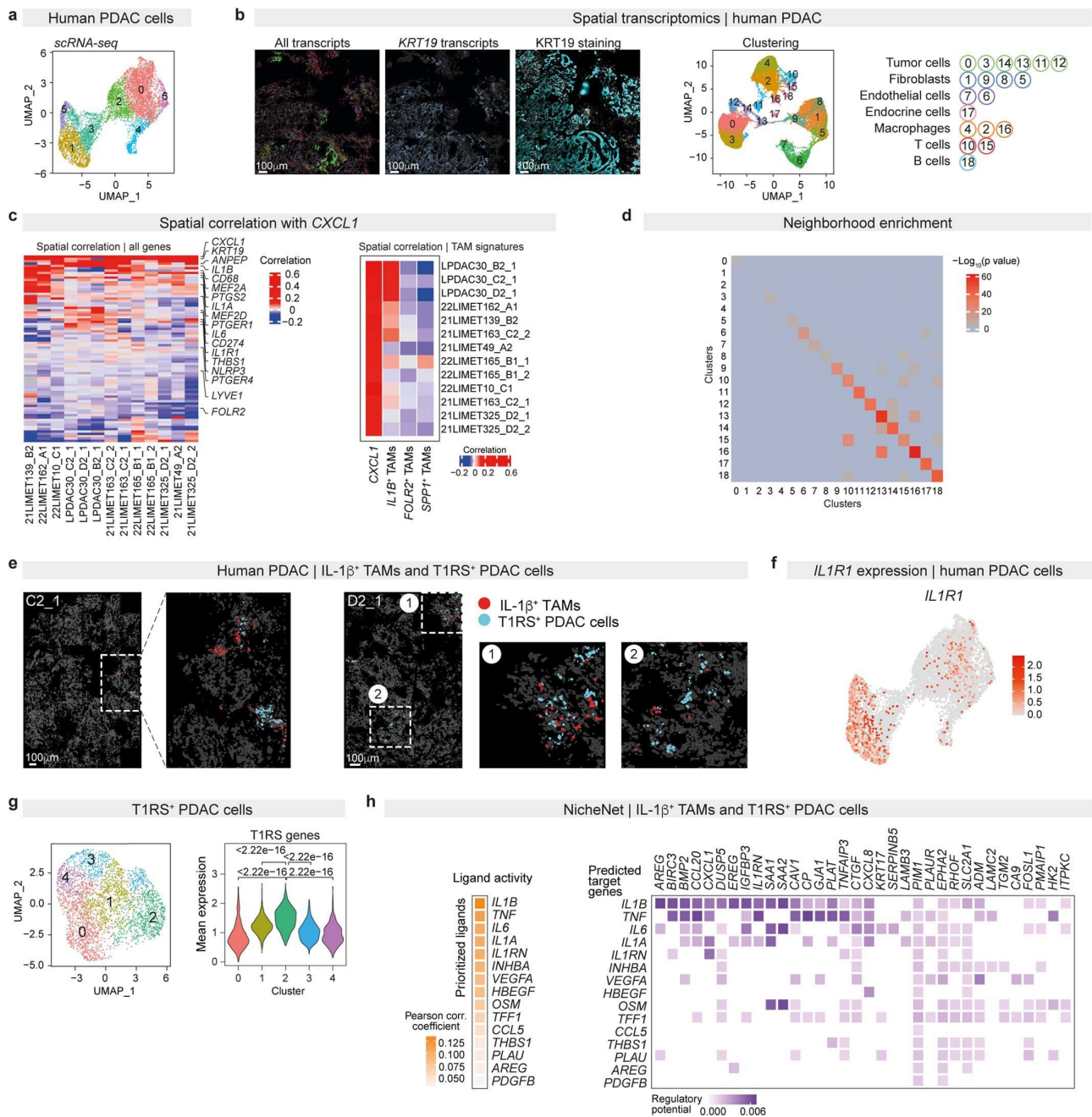
Extended Data Fig. 10: Spatial analyses of IL-1β+ TAMs and T1RS+ PDAC cells.

a, UMAP plot of scRNA-Seq data of PDAC cells from chemotherapy-naïve patients. Colors and numbers indicate cluster identity. b, Left panels. Selected region of interest (LPDAC30 B2_1) showing expression (Molecular Cartography) of all (563,761) detected transcripts or KRT19, as well as signal intensity (IF staining) of KRT19. Right panels. UMAP of spatial gene expression data (Molecular Cartography) of cells from all sections collected from patient LPDAC30. Colors and numbers indicate cluster identity and corresponding annotations. c, Heatmaps of spatial correlation of gene expression (see Methods) with CXCL1 of genes of the spatial transcriptome panel (left) or of marker genes of TAM subsets (right). d, Heatmap of spatial neighborhood significance between the indicated clusters (see Methods). e, Selected regions of interest (LPDAC30 C2_1, left. LPDAC30 D2_1, right) showing co-localization of IL-1β+ TAMs

(red) and T1RS+ PDAC cells (light blue) in spatial gene expression analyses. Numbers indicate insets and their magnifications. f, UMAP showing expression (scRNA-Seq) of IL1R1 in PDAC cells from chemotherapy-naïve patients. g, UMAP of scRNA-Seq data (left) and violin plot showing mean expression of T1RS genes (right) of PDAC cells selected for pseudotime analysis. Colors and numbers indicate cluster identity. Significance is computed by two-sided Mann-Whitney test. h, Heatmaps (NicheNet) of ligand activity (Pearson correlation coefficient) of top-ranking ligands expressed by IL-1β+ TAMs (left) and their regulatory potential on predicted target genes expressed by T1RS+ PDAC cells (right).